Analysis of the lightfield of a test facility to characterize the JUNO PMTs

Untersuchung zum Lichtfeld eines Teststandes zur Charakterisierung der JUNO PMTs

by

Simon Reichert

born on

December 3, 1994

Bachelor thesis in physics

Universität Hamburg

November 7, 2016

1. reviewer: Prof. Dr. Caren Hagner
2. reviewer: Dr. Björn Wonsak

Abstract

With the JUNO experiment, the neutrino mass hierarchy of the mass eigenstates should be determined. This results in special requirements for the 20 kt detector and the 20000 20″ PMTs. Therefore, among other things, a test facility with the ability of mass testing is needed to characterize the PMTs.

Each of the test chambers has a cylindrical cardboard tube, where on one ending the PMT sits and on the other a light source. The purpose of the tube is to shape the illumination of the PMT and therefore it is partially covered with reflecting material. Within the scope of this Bachelor-thesis, a simulation was developed to find the best setup for the tube.

Due to the results of the simulation, the 60 cm long tubes are laminated on the PMT's end of the tube with 30 cm Tyvek, which is a highly reflective scattering material.

Zusammenfassung

Mit dem JUNO Experiment soll die Neutrino-Massenhierarchie der Masseneigenzustände bestimmt werden. Dies stellt besondere Anforderungen an den 20 kt Detektor und die 20000 20″ PMTs. Deswegen wird unter anderem ein Teststand für einen Massentest zur Charakterisierung der PMTs benötigt.

Jede der Testkammern enthält eine zylinderförmige Papprolle, an deren Enden sich der PMT und eine Lichtquelle befinden. Die Rolle hat die Aufgabe die Beleuchtung des PMT zu formen und ist daher zum Teil mit reflektierendem Material beschichtet. Für die genaue Zusammensetzung wurde im Rahmen dieser Bachelor-Arbeit eine Simulation entwickelt, um das beste Setup in der Röhre zu finden.

Letztlich werden aufgrund der Ergebnisse der Simulation die 60 cm langen Röhren auf der PMT Seite der Röhre mit 30 cm Tyvek, einem hoch reflektierendem streuenden Material, beklebt.

Contents

1. Introduction

Neutrinos are very hard to detect since they only interact via weak interaction. Nevertheless, much effort is put into the research of them because of the open issues in neutrino physics and the importance of them for other fields of particle physics, but also cosmology and astrophysics.

Here comes into play the multi-purpose reactor neutrino experiment JUNO, located located near Kaiping, China the JUNO detector consists of 20 kt liquid scintillator and is surrounded by about 20000 20″ photomultiplier tubes (PMT). In the detector, neutrinos are detected by inverse beta decays, which create a unique light signature in the PMTs.

The main goal is the determination of the neutrino mass hierarchy, i.e. the ordering of the masses of the mass eigenstates. Furthermore, an overall improvement is aimed for the accuracy of the oscillation parameters, which characterize the neutrino oscillations, i.e. the transition between the three neutrino flavors e, μ and τ. To reach the ambitious goals, especially the mass hierarchy, a very high energy resolution better than 3% at 1 MeV is required, which was never reached with this detector type up to now. Therefore, the JUNO detector has to comply with high standards.

The characteristics of all 20000 20″ PMTs, arranged that they will cover more than 75% of the detector's surface, have to been known exactly. Thus, the performance of the PMTs will be tested in a test facility that is developed specially for large scale testing of the JUNO PMTs. The test facility consists of a single light source pointing onto the PMT while the whole implementation is bound by a cylindrical tube with the purpose of shaping the lightfield onto the PMT.

An important parameter of PMTs is the photon detection efficiency (PDE) which is the probability of an incoming photon to be detected. As only the average PDE can be determined by the test facility, it is needed to set up the tubes in a way that the illumination of the PMTs is as homogeneous as possible to achieve consistent and reliable results for the PDE. Hence, the tube is partially covered with reflective material in a way that has to be found with a simulation. The simulation replicates the test facility as close as possible. The setup will be optimized in terms of both homogeneity and running time of the photons. The final setup will then be implemented in the test facility. This simulation was developed and is discussed in this thesis as well as its results.

The assumptions of the simulation are discussed in chapter 3. The geometry of the simulated test facility is accurately adjusted with respect to the actual implementation as described in section 3.1. The photons are simulated using geometrical optics (introduced in section 3.3) rather than using the complex Geant4 simulation platform. As explained in section 3.7, this simplification is suitable especially in the context of the computational effort.

The structure of the simulation is roughly introduced in chapter 4, where also first results of the simulation are shown and made plausible. Finally, the results are discussed in chapter 5. The best setup, that will also be used in the actual implementation, is concluded in section 5.4.

2. Motivation

This chapter motivates the physical background of JUNO and the experiment itself as the basis for this Bachelor-thesis. After a short introduction to the Standard Model of particle physics in section 2.1, the focus is placed on neutrinos (section 2.2) and their properties, e.g. the neutrino oscillations (section 2.2.1). The JUNO experiment will be introduced next in section 2.3. Besides the detector and its goals, the functionality of PMTs and the test facility to characterize the JUNO PMTs will be explained.

2.1. Standard Model

The Standard Model of particle physics (SM), schematically shown in figure 2.1, combines theories about the known elementary particles and their fundamental interactions excluding gravity. It is considered as one of the biggest achievements in physics of the last century and is regarded as "the theory of almost everything." This overview is based on [32] and [46].

The SM contains 17 particles and the corresponding antiparticles. They are sorted in three groups, quarks, leptons and gauge bosons, and the Higgs boson [10], which is not discussed in this thesis furthermore.

The strong interaction is described in the quantum field theory *quantum chromodynamics* (QCD) which has a SU(3) symmetry. It predicts a new quantum number, the color charge and $3 \otimes \bar{3} = 8 \oplus 1$ gluons, a color charged octet and a color neutral singlet, which does not participate in the interaction. The gluon g is the gauge boson of the strong interaction, coupling only with quarks (up u, down d, charm c, strange s, top t, bottom b) and other gluons. The gluon has no electric charge, no mass and a spin of 1. By color confinement, quarks can only appear in bound color neutral systems. This also reduces the range of the strong interaction to a few fm, although the gluon is massless. The strong interaction conserves all relevant quantum numbers.

The gauge boson of the electromagnetic interaction is the photon γ, which has, as well as the gluon, no mass and no electrical charge and a spin of 1. It interacts with all charged

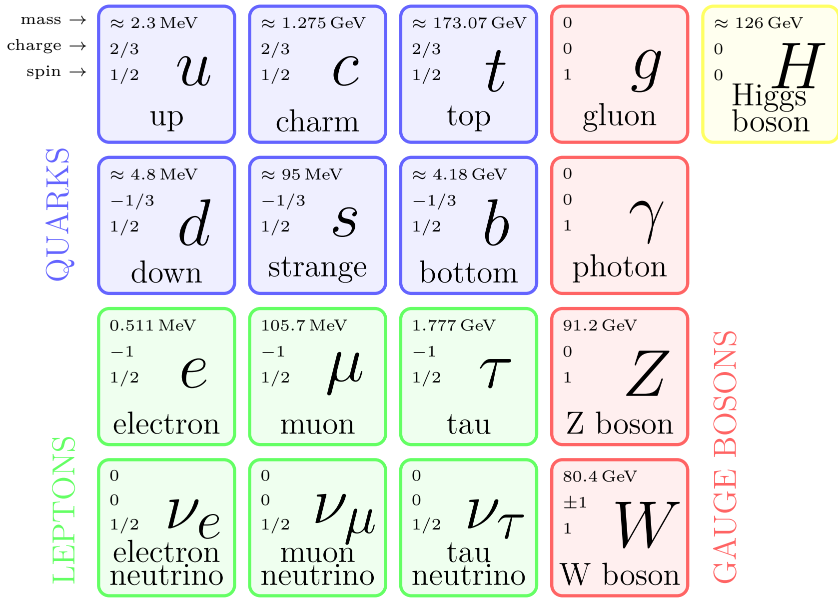

Figure 2.1.: Scheme of the Standard Model of particle physics. All units are given in natural units.

particles including the quarks, the charged leptons (electron e, muon μ, tau τ) and the $W^{\pm}$ boson (electroweak interaction) and its range is infinite. The electromagnetic interaction conserves the same quantum numbers as the strong interaction except for the isospin I. It is described in the quantum electrodynamics (QED).

The weak interaction appears either in a charged-current interaction (CC) or a neutral-current interaction (NC). The CC interaction is conveyed by the $W^{\pm}$ boson, while the Z^0 boson is the gauge boson of the NC interaction. All fermions, thus all leptons (including the neutrinos electron neutrino ν_e, muon neutrino ν_μ, tau neutrino ν_τ) and quarks participate on the weak interaction. Additionally, the photon couples with the $W^{\pm}$ boson. The name "weak" is not caused by the coupling constant (i.e. the strength of the coupling between gauge boson and corresponding charge), which is similar to the one of the electromagnetic interaction. Instead, the high masses of the Z^0 and $W^{\pm}$ bosons reduce the range extremely ($\sim 10^{-18}$ m). Except for some basic quantum numbers like the energy E, the momentum $\mathbf{p}$, the angular momentum $\mathbf{L}$ and the electrical charge Q, most of the quantum numbers are not conserved in the weak interaction. Especially the quark flavor can be changed since the mass eigenstates and the flavor eigenstates do not coincide. This is described with the CKM-matrix [37, 46]. The electromagnetic and the weak interaction are mathematically described combined in the electroweak interaction by a $SU(2) \times U(1)$ symmetry, that predicts the gauge bosons ($W^{\pm}$, Z^0 bosons and photon).

2.2. Neutrinos

Neutrinos are particles that only interact via weak interaction because they are massless and have no electrical and color charge in the Standard Model. As neutrinos are of special interest for this work, they are introduced in detail in this section.

Before the neutrino was discovered, the β decay was assumed to be a two body decay of the neutron n in a proton p and an electron e with the reaction

$$n \to p + e, \tag{2.1}$$

while the energy spectrum of the created electron was measured to be continuous. This indicated that the energy conservation and the angular momentum, too are violated. After most possible solutions have been rejected, Wolfgang Pauli proposed an additional unknown undetectable (massless and no electrical charge) particle involved. After the discovery of the neutron, Enrico Fermi published a complete theory about the β decay with the reaction

$$n \to p + e^- + \nu_e, \tag{2.2}$$

and named the new particle neutrino ν_e [15, 46].

The electron antineutrino $\bar{\nu}_e$ was discovered 23 years later in 1956 in the Cowan-Reines neutrino experiment with the inverse β decay [11]:

$$p + \bar{\nu}_e \to n + e^+, \tag{2.3}$$

whose Feynman diagram is shown in figure 2.2. For this discovery Frederick Reines was honored with the Nobel Prize in Physics in 1995.

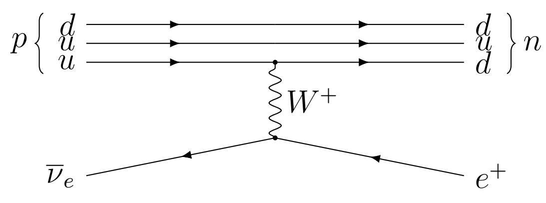

Figure 2.2.: Feynman diagram of the inverse β decay, that is used in the JUNO detector to detect the reactor electron antineutrinos. The time axis is horizontally.

Jack Steinberger, Melvin Schwartz and Leon Max Lederman detected the muon neutrino in 1962 with the first neutrino beam made in an accelerator [12] and received the Nobel Prize in Physics in 1988.

With the discovery of the tau particle τ in 1975, physicists also expected a tau neutrino generation, that was first directly observed in 2000 by the DONUT experiment [9, 31].

In the Standard Model, neutrinos do not have a mass and charge. Modern measurements verified neutrino oscillations and implied a non zero rest mass for the neutrinos. Neutrino oscillations allow, similar to the flavor changes of quarks via the CKM matrix, neutrinos to transform into another flavor. They are introduced in the next section 2.2.1.

Up to now it is unknown, whether the neutrino is a Dirac, i.e. the neutrino and the antineutrino are distinct, or a Majorana particle, i.e. neutrino and antineutrino are the same particle. The search for the neutrinoless double β decay can possibly clarify this question.

As there are still many unsolved questions left, the neutrino is an interesting object of recent research.

2.2.1. Neutrino oscillations

The first measurements of the flux of solar neutrinos in the late 1960s in the Homestake Experiment by Ray Davis and the calculations of the flux of John N. Bahcall revealed a huge deficit of about one third to one half compared to the predictions of the Standard Solar Model [13, 17]. In 2002 Ray Davis and Masatoshi Koshiba, constructor of the Kamiokande detector, won the Nobel Prize in Physics for the precise measurement of the solar neutrino flux.

The combined flux of all neutrino flavors was measured in the Sudbury Neutrino Observatory (SNO) detector and resulted in the electron neutrino flux which was predicted by the Standard Solar Model. This indicates a transition between the flavors, the neutrino oscillations, which are introduced based on [2, 37, 46] in the following.

Similar to the quarks the flavor eigenstates (that couple to the $W^{\pm}/Z^0$ bosons) and the mass eigenstates do not coincide. The flavor eigenstates ν_α with $\langle\nu_\alpha|\nu_\beta\rangle = \delta_{\alpha\beta}$ can then be written as superposition of the mass eigenstates ν_i with $\langle\nu_i|\nu_j\rangle = \delta_{ij}$ as

$$|\nu_\alpha\rangle = \sum_i U_{\alpha i} |\nu_i\rangle \tag{2.4}$$

by using a unitary mixing matrix U ($U^\dagger U = I$, where I is the identity matrix). Roman indizes $i, j, \ldots$ denote the mass eigenstates, while Greek indizes $\alpha, \beta, \ldots$ stand for the flavor states.

The mass eigenstates are stationary and evolve in time t:

$$|\nu_i(x,t)\rangle = \mathrm{e}^{-\mathrm{i}E_i t} |\nu_i(x,0)\rangle \,, \tag{2.5}$$

where

$$|\nu_i(x,0)\rangle = \mathrm{e}^{\mathrm{i}px} |\nu_i\rangle \,, \tag{2.6}$$

with E_i being the energy of the mass eigenstate, p being the momentum and x the position. Here, the assumption of a relativistic neutrino

$$E_i = \sqrt{m_i^2 + p_i^2} \simeq p_i + \frac{m_i^2}{2p_i} \simeq E + \frac{m_i^2}{2E}, \tag{2.7}$$

for $p \gg m_i$ and $E \approx p$ as neutrino energy, that was emitted at $t = 0$ by a source positioned at $x = 0$ was used. Neutrinos can be only produced and detected as flavor states, since only these couple with the gauge bosons of the weak interaction. When a neutrino with the flavor ν_α is emitted at $t = 0$, it develops in time to a state

$$|\nu(x,t)\rangle = \sum_i U_{\alpha i} \mathrm{e}^{-\mathrm{i}E_i t} |\nu_i\rangle = \sum_{i,\beta} U_{\alpha i} U^*_{\beta i} \mathrm{e}^{\mathrm{i}px} \mathrm{e}^{-\mathrm{i}E_i t} |\nu_\beta\rangle. \tag{2.8}$$

If the masses of two neutrino states differ, $\Delta m^2_{ij} := m_i^2 - m_j^2 \neq 0$, the phase factor in equation (2.8) differs for the summands and therefore the final state in the detector does not equal to the initial flavor. A conversion between the flavor states $\nu_\alpha \to \nu_\beta$ is possible. For the three flavors e, μ and τ the transition probability is given by

$$\begin{aligned} P(\alpha \to \beta) &= |\langle \nu_\alpha | \nu_\beta \rangle|^2 \\ &= \delta_{\alpha\beta} - 4 \sum_{j>i} U_{\alpha i} U_{\alpha j} U_{\beta i} U_{\beta j} \sin^2\left(\frac{\Delta m^2_{ij}}{4} \frac{L}{E}\right), \end{aligned} \tag{2.9}$$

where $L = x = ct$ is the distance between the source and the detector and CP-invariance is assumed. With fixed L/E the oscillation frequency only depends on the mass difference between the neutrino states. $U := U_{\mathrm{PMNS}}$ is the Pontecorvo-Maki-Nakagawa-Sakata matrix (PMNS matrix), which can be parametrized by

$$U_{\mathrm{PMNS}} = \begin{pmatrix} c_{12}c_{13} & s_{12}c_{13} & s_{13}\mathrm{e}^{-\mathrm{i}\delta_{\mathrm{CP}}} \\ -s_{12}c_{23} - c_{12}s_{23}s_{13}\mathrm{e}^{-\mathrm{i}\delta_{\mathrm{CP}}} & c_{12}c_{23} - s_{12}s_{23}s_{13}\mathrm{e}^{-\mathrm{i}\delta_{\mathrm{CP}}} & s_{23}c_{13} \\ s_{12}s_{23} - c_{12}c_{23}s_{13}\mathrm{e}^{-\mathrm{i}\delta_{\mathrm{CP}}} & -c_{12}s_{23} - s_{12}c_{23}s_{13}\mathrm{e}^{-\mathrm{i}\delta_{\mathrm{CP}}} & c_{23}c_{13} \end{pmatrix} \times \begin{pmatrix} \mathrm{e}^{-\mathrm{i}\rho/2} & 0 & 0 \\ 0 & \mathrm{e}^{-\mathrm{i}\sigma/2} & 0 \\ 0 & 0 & 1 \end{pmatrix}, \tag{2.10}$$

where $c_{ij} = \cos(\theta_{ij})$, $s_{ij} = \sin(\theta_{ij})$, θ_{ij} are the mixing angles that define the amplitude of the oscillations, δ_{CP} is the Dirac CP violating phase and ρ and σ are the Majorana CP violating phases, which are only unequal 1 if the neutrino is a Majorana particle. The Majorana phases do not affect the neutrino oscillations. CP-invariance states that physics does not change, when the charge (C) and all directions (P) are reversed. For CP-violation, this principle does not hold. The current values for the parameters of the PMNS matrix and the differences of the squared masses of the mass eigenstates are summarized in table 2.1.

For the first experimental discovery of neutrino oscillations and therefore for solving the solar neutrino problem, Arthur McDonald of the Sudbury Neutrino Observatory Institute (SNO) and Takaaki Kajita of Super-Kamiokande were honored the Nobel Prize in Physics in 2015.

Table 2.1.: Current values oscillation parameters for the normal ($m_1 < m_2 < m_3$) and inverted ($m_3 < m_1 < m_2$) hierarchy. The values are given in the 1σ range [2].

Hierarchy	Δm^2_{21} $[10^{-5}\,\mathrm{eV}^2]$	$\lvert\Delta m^2_{31}\rvert$ $[10^{-3}\,\mathrm{eV}^2]$	$\sin^2\theta_{12}$ $[10^{-2}]$	$\sin^2\theta_{13}$ $[10^{-2}]$	$\sin^2\theta_{23}$ $[10^{-1}]$	$\frac{\delta_{\mathrm{CP}}}{180^\circ}$
normal	7.32-7.8	2.41-2.53	2.91-3.25	2.15-2.54	4.14-4.70	1.12-1.77
inverted	7.32-7.8	2.34-2.48	2.91-3.25	2.18-2.59	4.24-5.94	0.98-1.60

As mentioned before, many questions regarding neutrinos are unsolved. This applies for the neutrino oscillations, too. Among other things, the absolute mass scale of the neutrinos (only the mass differences are measured nowadays), the Dirac CP violating phase δ_{CP} and the Majorana CP violating phases ρ or σ, that are added to the PMNS-matrix (2.10) and the question whether the neutrino happens to be a Majorana particle, are open issues of massive neutrinos. Furthermore, additional light and heavy sterile neutrino flavors are searched [2]. Sterile neutrinos are neutrinos that do not interact via

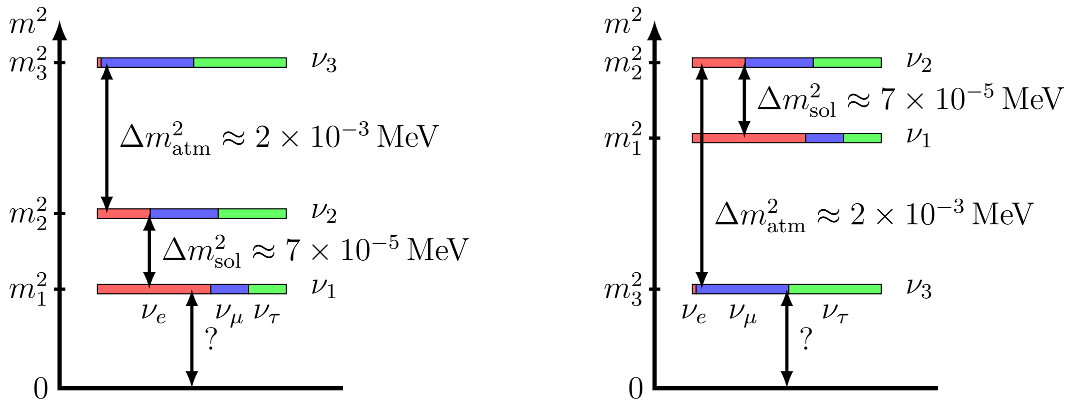

(a) Normal mass hierarchy **(b)** Inverted mass hierarchy

Figure 2.3.: Comparison of normal and inverted mass hierarchy. It is $\Delta m^2_{21} \sim \Delta m^2_{\text{sol}} \gg \Delta m^2_{31} \sim \Delta m^2_{32} \sim \Delta m^2_{\text{atm}}$, where m^2_{sol} and m^2_{atm} denote the squared mass differences for the neutrinos that dominate the oscillations for the neutrinos that originate from the Sun and atmosphere, respectively [33].

the fundamental interactions of the Standard Model (strong, weak and electromagnetic) but only via gravity (and potentially via yet unknown interactions).

Especially the mass hierarchy, i.e. the ordering of the masses of the three mass eigenstates ν_1, ν_2 and ν_3 has to be found. As the sign of Δm^2_{21} is positive but only the absolute value of Δm^2_{31} is determined, there are two possible orderings left, the normal hierarchy with $m_1 < m_2 < m_3$ and the inverted with $m_3 < m_1 < m_2$ (see figure 2.3). The mass hierarchy has a huge impact on important processes in particle physics, astrophysics and cosmology. Therefore, much effort is put into researching the mass hierarchy. The JUNO experiment, that is introduced in the next section, is expected to give answers to these questions [2].

2.3. The JUNO experiment

The Jiangmen Underground Neutrino Observatory (JUNO) is an upcoming multi-purpose liquid scintillator neutrino experiment located near Kaiping in the Chinese province Jiangmen and was proposed in 2008. The location of the experiment is shown in figure 2.4. Having a distance of roughly 53 km to the nuclear power plants in Yangjiang and Taishan, it was designed to determine neutrino mass hierarchy and precisely measure oscillation parameters via inverse β-decay detection (see formula (2.3) and figure 2.2). In addition to the reactor neutrinos, the 20 kt liquid scintillator detector of JUNO will also observe supernova neutrinos and study atmospheric, solar

Figure 2.4.: Location of the JUNO detector. The approximate distance to the Taishan and Yangjiang NPPs is 53 km. The experiment is located near to Kaiping and Hongkong. *Source:* `http://umap.openstreetmap.fr/en/` © OpenStreetMap contributors, licensed under the Creative Commons Attribution-ShareAlike 2.0 license (CC BY-SA).

and geoneutrinos. To reduce background, the detector has a rock overburden of 700 m. While the construction started in 2015, completion and first measurements are expected to run in 2020.

2.3.1. Goals and expectations

The main goal of JUNO is to determine the mass hierarchy of the neutrinos. In particular the energy spectrum of the reactor antineutrinos should be measured precisely and therefore the probability for a transition between an electron antineutrino to an electron antineutrino, i.e. the probability for an reactor neutrino to remain in its flavor, $P(\bar{\nu}_e \to \bar{\nu}_e)$ is determined. With equation (2.9) and the PMNS-matrix (2.8) this is

$$\begin{aligned} P(\bar{\nu}_e \to \bar{\nu}_e) &= 1 - P(\bar{\nu}_e \to \bar{\nu}_\mu) - P(\bar{\nu}_e \to \bar{\nu}_\tau) - P(\bar{\nu}_\mu \to \bar{\nu}_\tau) \\ &= 1 - \sin^2(2\theta_{12}) c_{13}^4 \sin^2(\Delta_{21}) - \sin^2(2\theta_{13}) \left[c_{12}^2 \sin^2 \Delta_{31} + s_{12}^2 \sin^2 \Delta_{32} \right], \end{aligned} \tag{2.11}$$

where $\Delta_{ij} = \frac{\Delta m_{ij}^2}{4} \frac{L}{E}$ [2].

Figure 2.5 shows the flux of electron antineutrinos from the reactors in the JUNO detector in arbitrary units plotted against the parameter L/E. The dashed line indicates the non oscillation spectrum, i.e. the distribution of electron antineutrinos emitted from the reactor in the direction of the detector. As L is known and E can be measured/reconstructed, the oscillation mainly depends on Δm_{21}^2, Δm_{31}^2 and Δm_{32}^2.

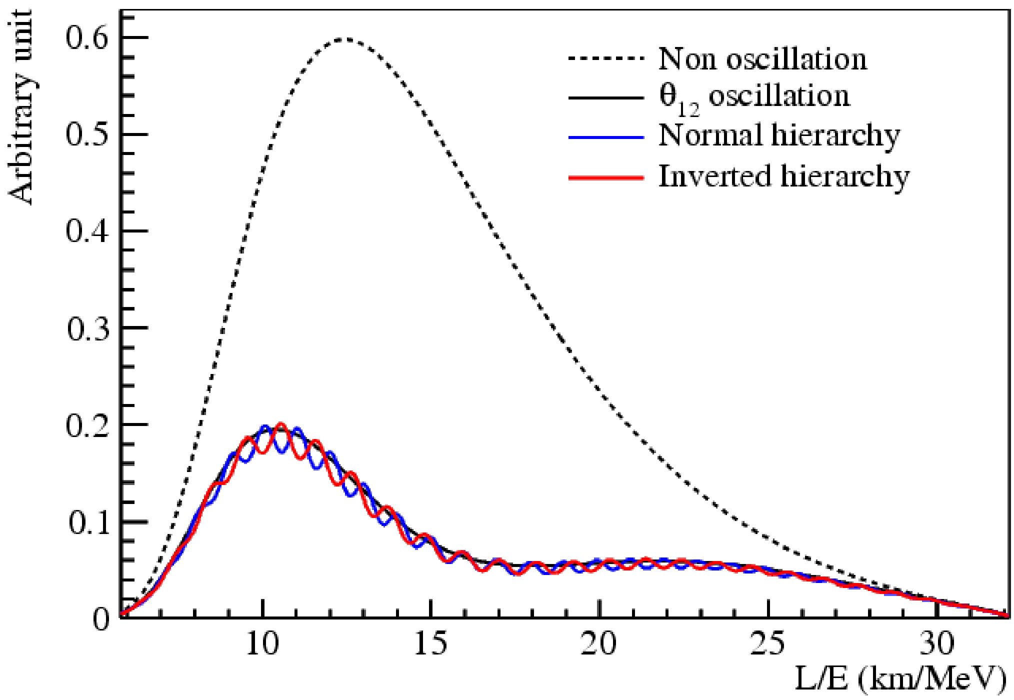

Figure 2.5.: Flux of electron antineutrinos in the JUNO detector. The dominating θ_{12} oscillation reduces the flux massively, while the normal or inverted hierarchy, respectively create oscillations with a significantly smaller amplitude and high frequency. With JUNO these differences should be resolved [30].

Δm^2_{21} is comparatively small, as can be seen in figure 2.3, and the corresponding $1 - P(\bar{\nu}_e \rightarrow \bar{\nu}_\mu)$ oscillation, displayed as the black continuous line, has a high amplitude and hence dominates the spectrum massively. Δm^2_{31} and Δm^2_{32} are of similar scale, while the amplitudes of the corresponding oscillations are relatively small and thus interfere with each other. Another oscillation with significantly higher frequency appears, whereby the exact frequency depends on the mass hierarchy. This leads to the blue and red curves for the normal respectively inverted hierarchy $P(\bar{\nu}_e \rightarrow \bar{\nu}_e)$ oscillations, shown in the figure. Roughly near to the maximum of the $1 - P(\bar{\nu}_e \rightarrow \bar{\nu}_\mu)$ oscillation ($L/E \approx 10\,\frac{\mathrm{km}}{\mathrm{MeV}}$), the normal and inverted hierarchy oscillations have a phase shift of about π. This difference can be measured, if the detector has a sufficient high energy resolution better than 3% at 1 MeV. Then the two hierarchies are distinguishable.

Furthermore, the extraordinary high energy resolution of the JUNO experiment should allow to measure the other parameters of the PMNS matrix Δm^2_{12}, Δm^2_{23} and $\sin^2(\theta_{12})$ precisely with the uncertainty being one order of magnitude improved compared to all previous experiments. Table 2.2 shows the expected precision in detail.

Table 2.2.: Current precision of the solar oscillation parameters in comparison to the desired precision of JUNO [2].

parameter	current precision	JUNO
Δm^2_{12}	3%	0.6%
Δm^2_{23}	5%	0.6%
$\sin^2(\theta_{12})$	6%	0.7%

Although reactor neutrinos are the main source of interest in order to determine the mass hierarchy, JUNO also detects solar, geo-, supernova and atmospheric neutrinos. By evaluating the data of these, other problems can be solved, too.

The examination of geoneutrinos provides information about the heat production inside the Earth to determine the distribution and amount of the different natural radioisotopes in the Earth's interior. With JUNO, the uncertainty of the total number of geoneutrinos can be reduced to probably 17%, while today it is 25% to 30% with the experiments KamLAND and Borexino [18]. Overall, this helps to improve geological models of the Earth.

As mentioned before, the solar neutrino problem was solved by the SNO experiment. The Borexino experiment measured wide parts of the solar neutrino spectrum. However, the flux of the CNO cycle, a nuclear fusion reaction in the Sun, which burns hydrogen into helium via carbon (C), nitrogen (N) and oxygen (O), is not verified to match with the theoretical predictions. This would allow to determine the metallicity of the Sun and therefore gives a better understanding of stars in general. Secondly, the MSW-effect (Mikheyev-Smirnov-Wolfenstein effect), an effect that influences neutrino oscillations in matter [43] can be verified by examination of the oscillation probability of neutrinos below 1 MeV energy. At these energies, the MSW-effect dominates the transition between flavors in matter.

Statistically, a core collapse supernova, which emits about 99% of the energy in form of neutrinos, happens every decade in our Milky Way. When a supernova occurs in the ten years of measurement, JUNO detects a vast amount of events (~ 5000 for a supernova in a distance of about 10 kpc from the Earth) within a few seconds. With the time course, the energy spectrum and the flavor composition of the neutrino burst, a better understanding of supernovae in general and the emergence of heavy elements in particular is gained.

Last but not least, JUNO will be used to hunt for new physics. To explain the matter antimatter asymmetry in the early universe, the proton decay is searched up to a sensitivity limit of 1.9×10^{34} years for the half-life, which comes close to the predicted scope of many Grand Unification Theories (GUT). In addition, JUNO searches for neutrinos which could originate from annihilation processes of dark matter in the Sun.

2.3.2. Detector

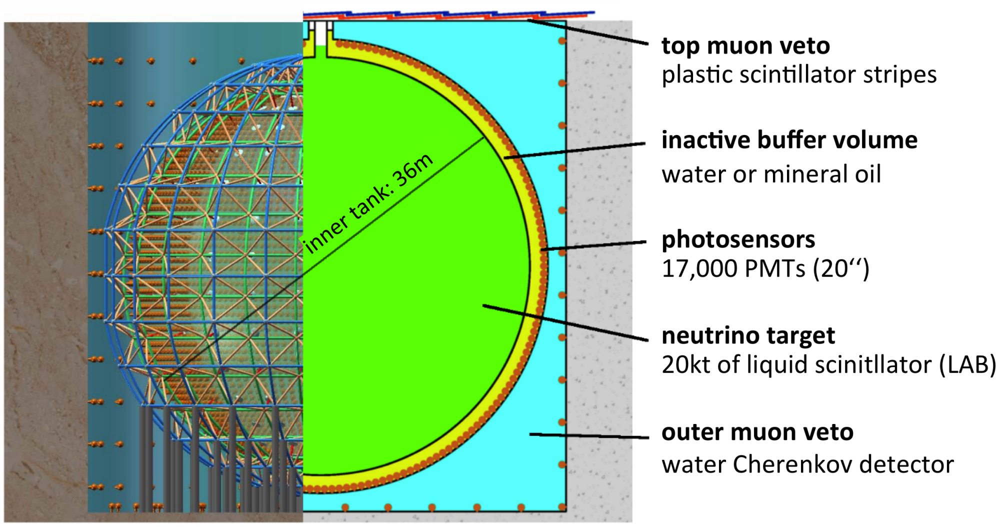

Figure 2.6.: Layout of the JUNO detector. The inactive buffer volume is specified to be water instead of mineral oil in a current version of the detector. [22].

The JUNO detector is shown in figure 2.6 schematically. It is a transparent sphere with a diameter of 35.4 m that consists of 20 kt highly transparent linear alkylbenzene (LAB) based liquid scintillator (LS). The LS is developed specifically for the JUNO experiment to provide a high attenuation length (> 30 m) and light yield (1100 photoelectrons per MeV) [14, 23, 45]. To keep the LS ultra pure as it is needed for the experiment, a special cleaning system is installed which is supposed to wash out impurities such as radioactive elements. The sphere is surrounded by approximately 17000 20″ high efficiency PMTs which should cover more than 75% of the sphere's surface [23].

Additional 2000 PMTs in a water Cherenkov veto around the actual detector are used to detect particles from the cosmic radiation to reduce the background. Moreover, there are plastic scintillator strips used as top muon veto above the detector [18].

The whole experiment is located 700 m below rocks and granite, which have a total mass water equivalent (MWE) of about 2000 m [38], to minimize the cosmic muon background events before they reach the detector.

Since JUNO is a low statistics experiment, it is important to know the background exactly. Therefore much effort is put into the examination and reduction of the background by e.g. using extensive simulations and running the experiment deep in the underground. Besides accidental background of radioactivity from several sources such as the rock, outer walls of the detector and the glass of the PMTs, one of the main sources of background are cosmic muons. The muons can either cross or shower inside the detector, where a high amount of energy is deposited. Furthermore, high energetic cosmic muons can interact with carbon atoms in the LS to form the cosmogenic isotopes ^{9}Li/^{8}He in nuclear spallation reactions. Their β^{-}-n decays have a similar signature as the inverse β decay, which is used to detect the electron antineutrinos. The cosmic muons is shielded by the overburden. In addition, its background is reduced by the muon veto around the detector. There are many additional sources of background, such as neutrinos from other sources than the reactor (e.g. geoneutrinos) and impurities in the liquid scintillator and other components of the detector [2].

In the detection process a reactor electron antineutrino interacts with a proton in the scintillator liquid with an inverse β decay (see formula (2.3) and figure 2.2). The formed positron carries most of the kinetic energy of the neutrino and quickly annihilates with an electron and the two created photons stimulate the scintillator molecules to emit photons with a specific wavelength (~ 420 nm in the case of the JUNO LS). This results in an immediate signal on the PMTs. The neutron on the other hand is captured by a proton after a short time (~ 200 µs) and emits a 2.2 MeV photon. Overall, this results in a unique signature for a neutrino event consisting of an immediate and a delayed signal. The expected rate for the inverse β decays is 40 per day [14].

JUNO is a liquid scintillator experiment, which means most of the detected light comes from the scintillation. Cherenkov radiation is principally formed, too, but only covers a minority of the light in the detector. Cherenkov radiation occurs, similar to the shock wave of supersonic flow, when a charged particle is faster than the speed of light in the medium. The light is sent as a cone in the direction of the particle. Beside liquid scintillator detectors, water-Cherenkov detectors are one of the most common in neutrino physics.

2.4. Test facility

In order to reach the high energy resolution in JUNO, the deployed PMTs have to comply with specific requirements. Therefore, a test facility is built to characterize and calibrate the PMTs. In this section, the functionality of PMTs (section 2.4.1) is explained and the test facility is introduced (section 2.4.2) as well as the simulation of the lightfield in this facility, which is the topic of this work.

2.4.1. PMT functionality

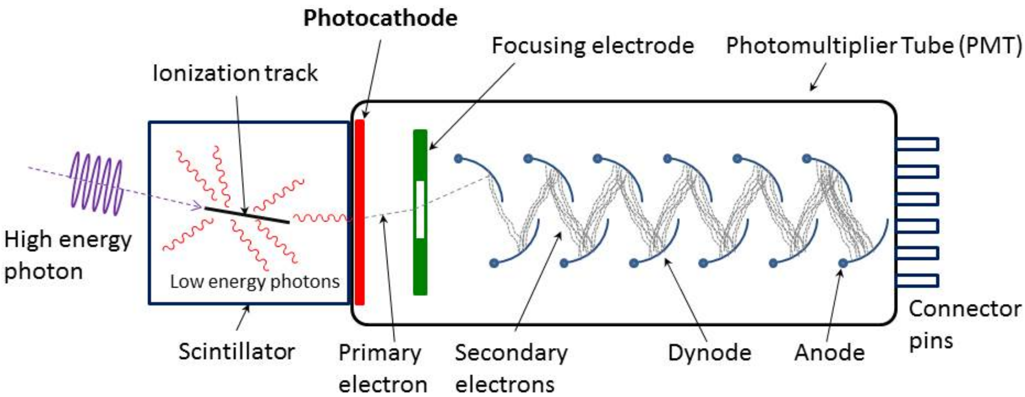

Figure 2.7.: Scheme of a PMT in combination with a scintillator [35].

Photomultipliers are devices to detect single photons by using the photoelectric effect and amplifying the signal. While there are many different types of photomultipliers such as silicon photomultiplier (SiPM) and photomultiplier tubes (PMTs), this section covers PMTs only.

Figure 2.7 shows the schematic layout of a PMT. The scintillator in front of the PMT does not belong to the PMT but produces the photons that should be detected by the PMT. The PMT has a photosensitive layer on a glass bulb, where the impinging photons with enough energy release a photo electron. The electron is accelerated and focused by the focusing electrode to strike the first dynode. The PMT has many consecutively ordered dynodes with a rising voltage to the next one ($\Delta V \sim 100\,\mathrm{V}$). This electron dissolves additional electrons out of the dynode and all of them are accelerated to the next dynode. Hence, the dynodes amplify the signal exponentially with the number of electrodes. In this way the PMT is able to detect single photons.

Important parameters to characterize a PMT are the photo detection efficiency (PDE) and the gain.

The photo detection efficiency is the fraction of photons that are detected by the PMT in proportion to the number of photons that hit the PMT. It is the product of the quantum efficiency (QE) and the collection efficiency (CE). The QE characterizes the photosensitive layer and the photocathode, by describing the fraction of photoelectrons produced by a photon. In general, the QE is a function of the position and the hit angle on the PMT surface. The needed QE for the JUNO PMTs is about 30 %, while the desired PDE is 27 %.

The CE on the other hand provides information about the fraction of photo electrons that are collected by the dynodes. As the electrons can be deflected by a magnetic field due to the Lorentz force, the CE depends on the magnetic field in the PMT. The PDE and QE are discussed later in detail in section 3.2.

The gain of the dynode is the number of secondary electrons that one photo electron produces. It describes the amplification of the signal by the dynodes. In most cases each of the electrodes in the dynode releases three to four secondary electrons for an incoming primary electron. A typical value for the gain is 10^6, while 10^7 is desired for the JUNO PMTs.

Photomultipliers have a wide scope of application. Besides detectors, particularly in the neutrino physics, photomultipliers are used e.g. in medicine by positron emission tomography (PET).

2.4.2. Test facility

To reach the ambitious goals of JUNO, the characteristics of the used PMTs have to be known very well. Therefore, a facility is implemented to measure the photo detection efficiency (and indirectly the quantum efficiency), the dark count rate, after pulsing and

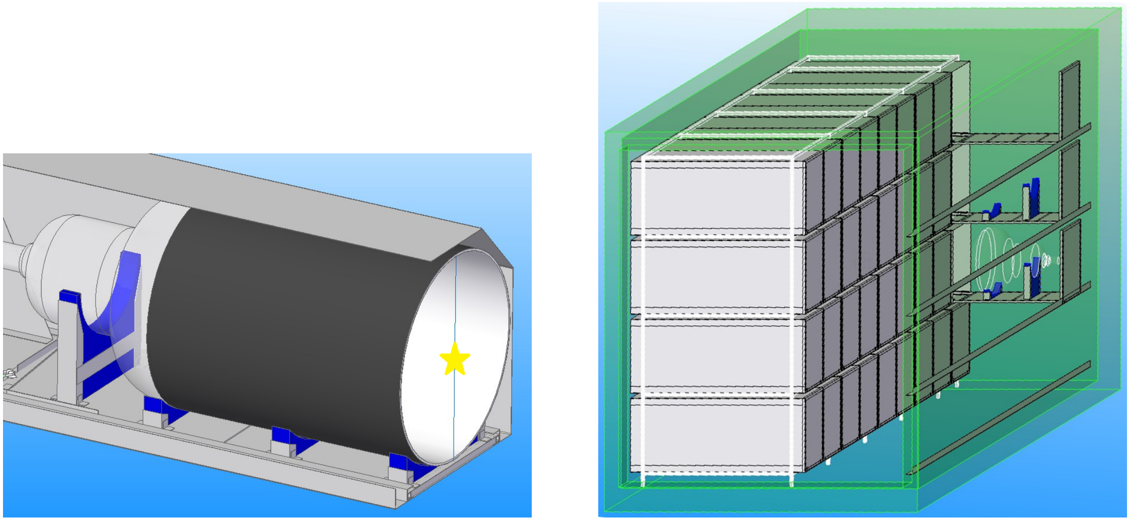

(a) Single test chamber (b) Container with 36 test chambers

Figure 2.8.: Scheme of one of the test container (right) and a single test chamber (left) [44].

many other parameters. In four temperature regulated containers, insulated from the Earth's magnetic field, 36 test chambers are implemented, each of them consisting of a tube with the PMT at one end and a light source on the other (see figure 2.8). The tube is partially covered with reflecting material to form the lightfield on the PMTs' surface.

The PDE test procedure is split into two phases. Phase I is an acceptance test, where PMTs, which do not comply with basic requirements on the photo detection efficiency are rejected and returned to the manufacturers of the PMTs. It is necessary to a test environment with consistent and stable conditions to get reproducible results. Comprehensible and fair specifications for the manufacturers of the PMTs are obligatory.

Phase II is used for a first calibration of the PMTs which passed phase I. Since the detector is filled with scintillator, while the test facility is filled with air, the exact realization of this phase is open currently. The lightfield in the tube is possibly adapted to replicate the expected lightfield in the actual detector. As this thesis occupies only phase I, phase II it is not discussed furthermore.

The PMTs are connected with an ADC (analog-to-digital converter), that counts the number of events in different channels corresponding to the height (charge or current) of the PMT signal.

In JUNO, and therefore also in the test facility, single photon events are detected mainly. This means only one photon hits the photomultiplier in most cases. Depending on crucial parameters of the PMT (e.g. photo detection efficiency and gain), the distribution of the hits per channel should visualize this in form of peaks. The dark rate, i.e. the number of events without a photon hitting the PMT, shows a huge peak for low channels that decreases exponentially for higher channels. The single photon events create an additional Gauss-distributed peak, which should be visible in the plot. For very good PMTs, a second or third significantly smaller peak could appear for multi photon events. The typical PMT signal is shown in figure 2.9.

While the moment of the signal t_s is known, the time of arrival t_0 of the photon on the photocathode is needed for the reconstruction of the events. Therefore, it is necessary to gather information about the typical temporal difference $\Delta t = t_s - t_0$. Instead of being constant, Δt has a characteristic distribution, which depends on the geometry of the PMT (curvature of the photocathode) and various other parameters. Thus, it is important to determine the average value and its variance σ. This variance is called transition time spread (TTS). The TTS is an important parameter for the PMTs that will be measured in the test facility. To do so, the time of arrival t_0 has to be known precisely to be able to determine the distribution of Δt. Hence, the setup of the test facility will also be optimized with respect to the variance of the running time of the photons.

The purpose of this work is to simulate the lightfield within the tube to find the best setup in terms of homogeneity of the illumination of the PMTs and other characteristics. This work focuses on phase I but of course the results are helpful for phase II, too.

Even though, the results of the simulation are appropriate to be taken into account to find the setup in the tubes for the second phase, this work focuses on the first one.

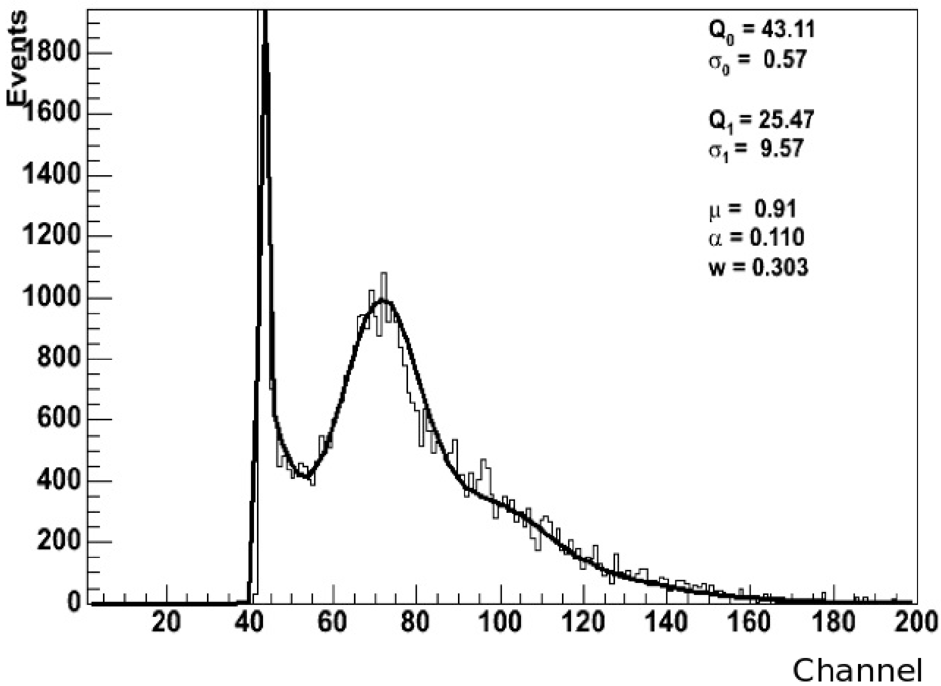

Figure 2.9.: Typical PMT signal, where the first huge peak is the pedestal (dark rate) and the second peak the single photoelectron event. The small peak for the two photoelectron events is faintly visible [7].

3. Theoretical background and assumptions of the simulation

With the simulation in this thesis, the best setup is searched for the test facility. This chapter discusses the assumptions and the theoretical background regarding the simulation in detail. In particular, the geometry of the PMT and the tube (section 3.1) and the materials on its walls (section 3.3) are introduced as well as the quantum efficiency (section 3.2), the light source (section 3.3.5) and different types of diffusers (section 3.4). Furthermore, the process of generating the random numbers (section 3.5) and transforming between different coordinate systems (section 3.6) is explained.

3.1. Geometry of the tube and PMT

In this section, the geometry of both the tube and the PMT is introduced. For a better overview, this section is divided into the geometry of the actual implementation (section 3.1.1) and the assumed geometry of the simulation (section 3.1.2). Furthermore, the importance of the running time is explained in section 3.1.3.

3.1.1. Actual test facility

Tube

The test facility is bounded by a cylindrical tube with a diameter $d = 502\,\mathrm{mm}$, which surrounds the photosensitive area of the PMT and the light source. The distance between the light source and the top point of the PMT is $490\,\mathrm{mm}$ and the overall length of the tube is $600\,\mathrm{mm}$. As a result of the uncertainty of the components in the test chamber, the tube does not close exactly with the PMT which leads to a gap of about $10 - 30\,\mathrm{mm}$ between the end of the tube and the PMT surface. Because of the open covers of the tube, photons can escape the tube in the test chamber, where all components are coated in black. The geometry is shown in figure 3.1.

PMT

Two kinds of 20″ PMTs are tested in the test facility, a customized version of the Hamamatsu R12860-50 PMT with a very similar geometry and the Northern Night Vision Technology MCP PMT. Both have similar but not exactly the same dimensions.

The glass bulb in the front has an almost spherical shape with an outwardly decreasing curvature radius and a diameter of about 508 mm. On this glass, the photo cathode and thus the photosensitive layer is deposited with a diameter of about 490 mm. The dimensions of the PMTs are shown in appendix B.1 and B.2.

3.1.2. Simulation

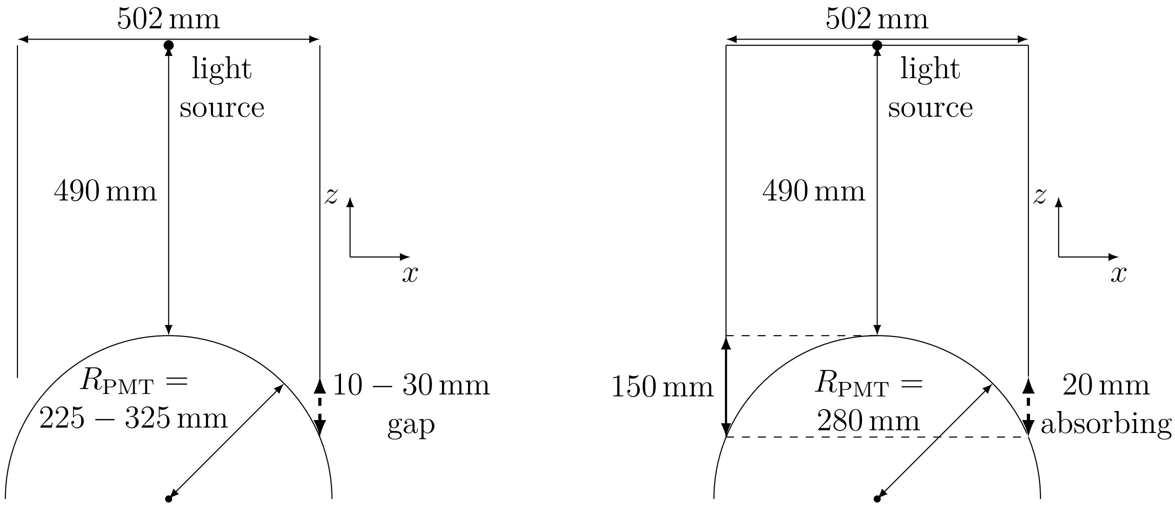

(a) Actual implementation

(b) Simulation

Figure 3.1.: Comparison between the geometry of the actual implementation and the geometry of the simulation. Cross section parallel to the xz plane.

Tube

The dimensions of the tube in the simulation are chosen close to the actual implementation. The diameter of the tube is $d = 502$ mm and the distance from the light source to the top point of the PMT is 490 mm.

Since all components surrounding the PMT and the tube are black, the gap between the tube's end and the PMT is implemented as an additional 20 mm length of the tube which is perfectly absorbing. To avoid the need to simulate the parts outside of the tube and PMT, the covers of the tube are closed and 100% absorbing, too. Thus, instead of escaping the tube, the photons are absorbed immediately.

The distance of the top point of the PMT and the point of contact of the tube on the PMT is 150 mm. Combined this results in a tube with a length of 640 mm. The assumed geometry is shown in figure 3.1.

PMT

As not all properties of the MCP PMT were known when the simulation was implemented, the simulation uses the geometry of the Hamamatsu PMT as a base for the PMT model.

The PMT is assumed a sphere with a photosensitive area shaped as a spherical segment. The radius can be determined by cutting the sphere at the point with the highest radius. The radius of the resulting circular segment regarding the actual numbers, is

$$R_{\mathrm{PMT}} = \frac{4h^2 + s^2}{8h} \approx 265\,\mathrm{mm} \tag{3.1}$$

where h is the height of 190 mm for the Hamamatsu PMT and 184 mm for the MCP PMT respectively, and $s = 508\,\mathrm{mm}$ the width of the circular segment (appendix B.1). Since the actual distance in the tube between the top point of the PMT and the point of contact of the tube and the PMT is about 150 mm instead of 180 mm for this radius, the radius of the simulated PMT is increased until this distance decreases to 150 mm. The new radius is

$$R_{\mathrm{PMT}} = 280\,\mathrm{mm}. \tag{3.2}$$

The geometry is schematically shown in figure 3.1.

3.1.3. Running time of photons

In the actual test facility, the photons should arrive one by one within a short definite time frame. Otherwise, if the uncertainty of the time of arrival is too high, the TTS of the PMT cannot be determined (see section 2.4.2). Therefore the variance of the running time should be taken into account for the selection of the setup. As the uncertainties of the components in the tube, especially the time resolution of the light source was not known at the time of implementation, the goal for variance of the running time is to stay below 1 ns.

The running time is calculated by adding the distances from one way point to another and dividing by the speed of light:

$$t = \frac{d}{\mathrm{c}}, \tag{3.3}$$

where t is the running time, d the total distance and c is the speed of light.

3.2. Photo detection efficiency and quantum efficiency

The quantum efficiency (QE) and the photo detection efficiency (PDE) are parameters to characterize a photomultiplier, which both give information about how well the PMT detects photons. Nevertheless, they have a slightly different meaning.

The quantum efficiency ξ is defined by

$$\xi = \frac{N_{\mathrm{pe}}}{N_{\mathrm{hits}}}, \tag{3.4}$$

where N_{hits} is the number of photons reaching the PMT and N_{pe} is the number of created photoelectrons. This means the probability of a photon to eject a photo electron in the photosensitive layer. The effective thickness of the photosensitive layer depends on the incidence angle of the hitting photon and due to the manufacturing process also on the location on the PMT. Thus the QE is sensitive to the incidence angle of the photon and the location of the hit.

The photo detection efficiency η, defined by

$$\eta = \frac{N_{\mathrm{det}}}{N_{\mathrm{hits}}} = \xi \cdot \chi, \tag{3.5}$$

where N_{det} is the number of detected PMT signals. Additionally, it takes into account the collection efficiency (CE) χ, which is the probability of the photocathode to catch a photo electron. This makes the total probability to detect a photon. A magnetic field perpendicular to the electron's path diverts the electrons due to Lorentz force and therefore influences the CE and PDE. The CE also depends on the incidence angle of the photon, as the initial direction of the ejected electron points in a similar direction as the photon due to the conservation of momentum.

In the test facility, the PDE is measured, while the QE can only be concluded by the PDE and information about the CE and the gain. In the actual PMT, the dependence of the incidence angle and hit position of the photon on the PDE are caused by both the QE and CE. As the simulation ends on the PMT surface, the PDE and QE are not distinguishable in this thesis. Therefore, the CE is set to 100% and only the PDE is used to characterize the PMT. A typical value for CE is 97% which justifies the assumption.

3.2.1. How to measure PDE and QE

The detection and quantum efficiency can be measured in several ways, in which a defined number of photons is sent on the PMT and the number of PMT signals is count. Then, the PDE can be determined with equation (3.5). The number of photo electrons and therefore the QE can be concluded by using the gain and CE (if known) with equation (3.4).

Two methods which are used in JUNO to characterize the PMTs are introduced below as an example.

Spatially resolved measurement of the PDE

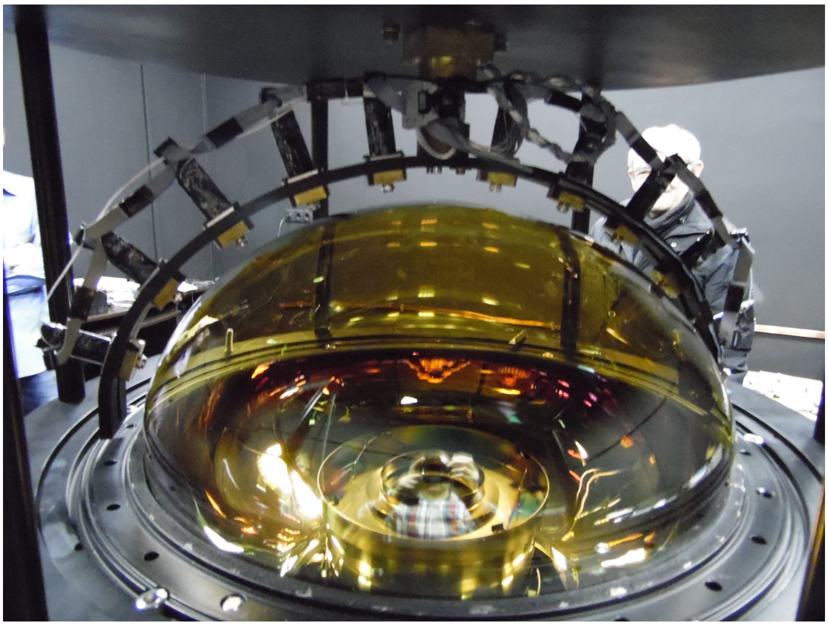

Figure 3.2.: Implementation of the spatially resolved method with a PMT installed [3].

In the first method, 5 to 12 LEDs (depending on the actual implementation) are placed on an arc directly above the PMT. The arc rotates in a 360° angle around the PMT to scan every point. This allows to measure the PDE distribution with a spatial resolution, that depends on the distance of the LEDs to the PMT surface and the impact of a wide variety of hit angles [3]. It is impossible to decide if inhomogeneities in the PDE are caused by the QE or by the CE.

The big downside of this method is the complicated setup. Thus, it is not suitable for mass characterization, as it is needed in the test facility, where a high amount of PMTs is tested simultaneously.

A few PMTs are tested with this method to calibrate the test facility that uses the second method.

Method of the test facility

The second method is actually used in the test facility. Here, a single LED is used as a light source, which is located opposite to the PMT on one end of a cylindrical cardboard tube. The tube is partly covered with reflective material and absorbing material and has the propose of forming the lightfield on the PMT.

The setup of the tube and light source is intended to produce a homogeneous illumination of the PMT, while simultaneously only one photon should hit the PMT in a short period of time (essentially the duration of the PMT signal). The goal is to reach a maximum deviation between the maximum and minimum illumination of less than 10%.

The comparatively easy implementation qualifies this method for the large scale testing of the PMTs. On the other side, it is not spatial resolved and therefore it only determine the average PDE of the PMT. The homogeneous illumination should ensure that every point on the photosensitive layer is weighted equally in the determination of the average PDE. See also section 2.4.2.

3.2.2. Conversion factor for the PDE

In order to calculate the PDE in the simulation with the total number of photons and the number of detected photons, a conversion factor is needed, which takes into account the fraction of emitted photons N_{total} that hit the PMT. Since the photo detection efficiency is given by $\eta = \frac{N_{\text{det}}}{N_{\text{hits}}}$ the conversion factor δ_{PDE} can be determined easily for a given scenario in the simulation:

$$\eta = \frac{N_{\text{det}}}{N_{\text{hits}}} = \delta_{\text{PDE}} \cdot \frac{N_{\text{det}}}{N_{\text{total}}} \tag{3.6}$$

$$\Leftrightarrow \qquad \delta_{\text{PDE}} = \frac{N_{\text{total}}}{N_{\text{hits}}}. \tag{3.7}$$

For the actual experiment a similar correction has to be made using PMTs with a known PDE distribution to calibrate the system. Here, a PMT that is identical in construction is used as a reference. The uncertainties of all components in the implementation are included in the correction.

3.3. Reflection, scattering and light source

The tube will be partially covered in reflective material and thus reflection (section 3.3.1) and scattering (section 3.3.2) is introduced in this section. Furthermore, the properties and model of Tyvek, which is actually used in the test facility is discussed in section 3.3.3.

3.3.1. Reflection

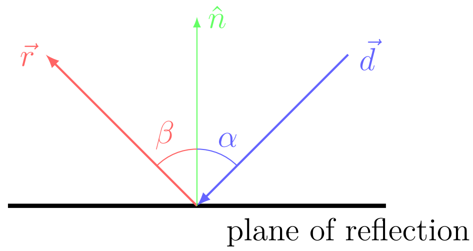

Figure 3.3.: Reflection on wall. The incident beam $\vec{d}$ with an incident angle α is reflected with a reflection angle β with $\alpha = \beta$. $\vec{r}$ is the reflected beam.

The law of reflection states, that the reflection angle equals to the angle of incidence. A short derivation (appendix A.1), which uses the orthogonal decomposition of the vector of incidence $\vec{d}$ and the reflection vector $\vec{r}$, leads to a simple formula for the reflection vector:

$$\vec{r} = \vec{d} - 2 \cdot \left\langle \vec{d}, \hat{n} \right\rangle \hat{n}, \tag{3.8}$$

where $\hat{n}$ is the normalized perpendicular to the plane of reflection. For rough reflecting surfaces an additional Gaussian blur appears around the direction of the reflection vector.

3.3.2. Scattering and Lambert's cosine law

Lambert's cosine law describes the ideal scattering of light on a surface. The luminance, i.e. the light intensity from an area element with respect to a certain direction, of a material, that obeys Lambertian reflectance, is constant [16].

Extended to the whole illuminated area, the luminous intensity, i.e. the light intensity in a certain direction, has a cosine shape due to projection of the illuminated area on the plane perpendicular to the observer.

The connection between the luminance and the luminous intensity is defined by

$$L_{\mathrm{v}} = \frac{\mathrm{d}I_{\mathrm{v}}}{\mathrm{d}A\cos\varepsilon}, \tag{3.9}$$

where L_{v} is the luminance, I_{v} is the luminous intensity, A is the illuminated area and ε is the angle of observation. Since the luminance is constant for Lambertian reflectance, this simplifies to

$$L_{\mathrm{v}} = \frac{I_{\mathrm{v}}}{A\cos\varepsilon}. \tag{3.10}$$

For the simulation, the crucial quantity is the luminance, as it only examines single photons that are only scattered on a single point and not an area. Thus every direction is equally probable for the ideal scattering.

There is no material that perfectly obeys Lambertian reflectance. However, some materials such as Tyvek, which is introduced in the next section, come close to it.

3.3.3. Tyvek

Tyvek, a registered trademark by DuPont, is a highly reflective material, which appears like paper in terms of look and feeling. It consists of small glued synthetic fibers. Tyvek is considered as a standard material to cover walls of particle physics detectors and is inter alia used in the Kamiokande experiment.

As a first approximation the Tyvek bidirectional reflectance distribution function (BRDF), which characterizes the reflection of a material, consists of a scattering part, that almost perfectly obeys the Lambert cosine law and a part with Gaussian reflection

[28]. Higher order effects are neglected in this simulation as they have a low impact on the results. The parameters in [28] are shown in table 3.1 for a wavelength of $\lambda = 325\,\text{nm}$. The fraction of reflected light increases with the angle of incidence, while the standard deviation σ of the Gauss part only varies slightly.

Table 3.1.: Values of [28] for the reflection and scatter parameter and the σ of the Gauss function for the reflection part, where θ_i is the angle of incidence, n_{scatter} and n_{reflect} the fraction of scattering and reflection, respectively and σ the standard deviation of the Gauss function (3.11).

θ_i [°]	n_{scatter}	n_{reflect}	σ [rad]
5	0.82±0.05	0.18±0.05	0.22±0.02
15	0.80±0.03	0.20±0.03	0.26±0.02
30	0.80±0.02	0.20±0.02	0.24±0.02
45	0.81±0.02	0.19±0.02	0.21±0.02
60	0.74±0.02	0.26±0.02	0.18±0.02
75	0.52±0.04	0.47±0.04	0.19±0.02

Tyvek is easy to handle and therefore, combined with the good optical properties (low absorption and reflection close to Lambertian scattering) used for the walls as the scattering material.

In this simulation Tyvek was implemented by using [28] as a base but simplifying the model.

The reflective fraction increases with the angle of incidence θ, as mentioned before. Although, a finer subdivision is needed for higher angles, here only three divisions are used:

- $0° < \theta < 45°$: $n_{\text{reflect}} = 0.2$, $\sigma = 2 \cdot 0.23\,\text{rad}$
- $45° < \theta < 65°$: $n_{\text{reflect}} = 0.3$, $\sigma = 2 \cdot 0.18\,\text{rad}$
- $65° < \theta < 90°$: $n_{\text{reflect}} = 0.5$, $\sigma = 2 \cdot 0.19\,\text{rad}$

where n_{reflect} is the fraction of reflected photons. n_{reflect} is overestimated a bit for the mid range of incidence angles but possibly underestimated for very high incidence angles (>80°). Testing the impact of this parameter showed that small changes do not have a huge impact on the hit distribution of the PMT. Since the reflection part causes a huge peak in the intensity on the PMT (see section 4.3.2), the overestimation of n_{reflect}

can be considered as a worst case scenario. In [28], σ varies between $0.19 \pm 0.02\,\mathrm{rad}$ for $\theta = 75°$ and $0.26 \pm 0.02\,\mathrm{rad}$ for $\theta = 15°$. The factor 2 is caused by the slightly different definition of the Gauss function in [28]

$$f(x) = \mathcal{N} \cdot \exp\left(-\frac{(x-\mu)^2}{8 \cdot \sigma^2}\right) = \mathcal{N} \cdot \exp\left(-\frac{(x-\mu)^2}{2 \cdot (2 \cdot \sigma)^2}\right), \tag{3.11}$$

where $\mathcal{N}$ is a normalization constant, x is the variable and μ the shift of the maximum of the Gauss function on the x-axis. In this thesis it is defined by

$$f(x) = \mathcal{N} \cdot \exp\left(-\frac{(x-\mu)^2}{2 \cdot \sigma^2}\right). \tag{3.12}$$

In general, reflection and scatting are considered separately in this thesis. A combined BRDF increases the computational effort massively. This is due to the fact that the relevant ROOT function internally calculates the integral of the distribution within a loop to normalize the function.

3.3.4. Reflection on the PMT surface

The surface of the PMT is slightly reflective with a dependency on the hit angle. The light can be reflected on the air-glass and the glass-photocathode boundaries as described in [27] and [41]. Up to an angle of about $\theta_i = 70°$ the reflection coefficient is almost constantly $n_{\mathrm{reflect}} = 0.2$ and increases rapidly for higher angles to reach $n_{\mathrm{reflect}} = 1$ for $\theta_i = 90°$. Due to simplicity the reflection coefficient in this simulation is approximated by a constant up to an incident angle of $\theta_i = 70°$ and a straight line for higher angles:

- $0° < \theta_i < 70° : \; n_{\mathrm{reflect}} = 0.2$
- $70° < \theta_i < 90° : \; n_{\mathrm{reflect}} = 0.04 \cdot \theta_i - 2.6$

The second part approximates the rapid growth of n_{reflect} as a linear function. Overall, the reflection on the PMT surface is a bit higher than in [41] but replicates the actual reflection function very well in this simple assumption. As described in chapter 5, the PMT is hardly hit in higher angles ($\gtrsim 75°$) which justifies this simple assumption even more. The comparison between the reflectance of [41] and the one implemented in the simulation is shown in figure 3.4.

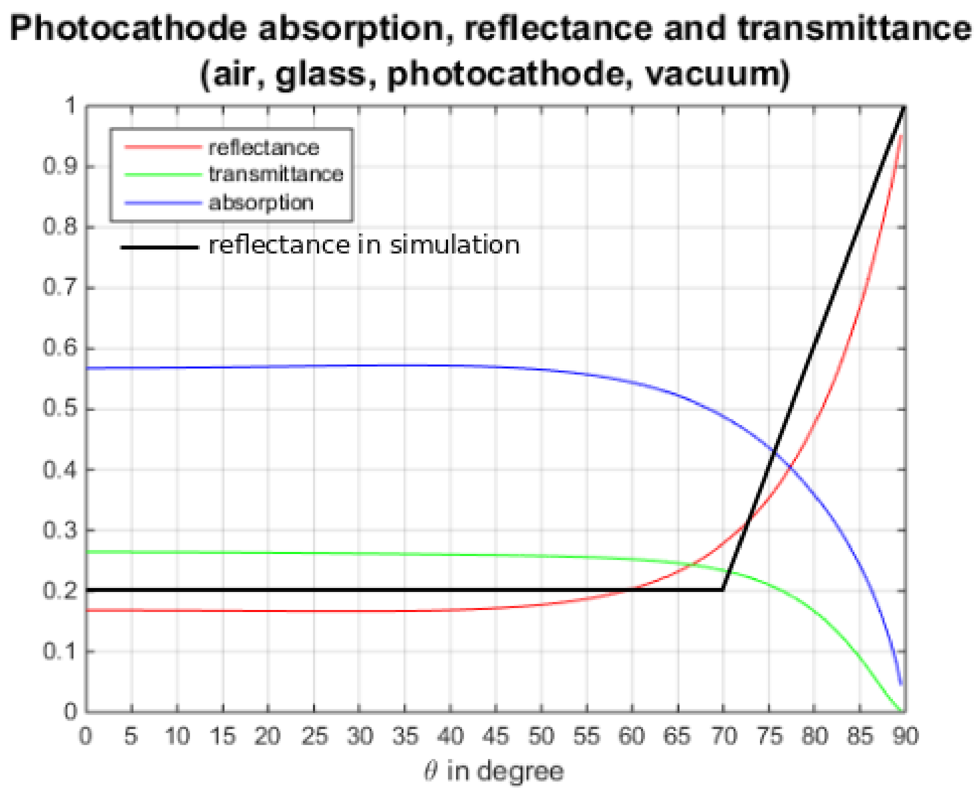

Figure 3.4.: Comparison of the reflectance of the approach in the simulation and [41].

3.3.5. Light source

The light source is one of the most important components of the test facility. The light of the single LED will be scattered by a diffuser to create an alomst isotropic source.

The implemented light source is a point source, that is located on top of the tube. It sends single photons in a uniformly distributed random direction within a cone with an arbitrary but fixed aperture angle.

Even though the aperture angle in a real light source is based on the full width at half maximum (FWHM) and transitions fluently from illuminated to unlighted areas, the lightfield of the source is approximated by sharp edges in the simulation. For higher aperture angles or small transition areas this assumption is tenable since only a small percentage of the photons has a higher angle to the optical axis in the real light source.

The actual light source is a possible source of errors as it can be shifted in all directions or tilted with respect to the cylinder axis of the tube. In the implementation it can be positioned with a uncertainty of a few mm, such that a simple shift in x or z direction does not have a noticeable impact. However, if the light source is tilted with respect to the cylinder axis, this can have a huge impact due to the distance of the light source to the PMT. A rough estimation showed, that a light source with 3 cm length can be adjusted with an inaccuracy below 1 mm which corresponds to a tilt of $\sim 1.91°$. As the tube has a cylindrical symmetry, it is sufficient for the determination of the impact to tilt the light source in one direction. Here, the positive x axis was chosen due to the simplest implementation.

3.4. Diffusers

There are different types of diffusers used in this simulation. All of them are assumed to have a transmission coefficient of $t = 0.9$, i.e. the fraction of photons that pass the diffuser.

Ideally, a diffuser scatters single photons isotropic in an opening angle of 180°. Even though such an ideal diffuser does not exist, the results allow a better insight in the general impacts of a diffuser on the hit distribution on the PMT.

However, to determine the homogeneity in the PMT distribution models for real diffusers are needed. In the following, two different implementations of diffusers in the simulation are introduced.

3.4.1. Holographic diffuser/ light shaping diffuser (LSD)

The output of the holographic diffusers, in particular the light shaping diffusers (LSD) of Luminit, have a well-defined angle of aperture β, that is given by

$$\beta = \sqrt{\alpha^2 + \Delta^2}, \tag{3.13}$$

where α is the opening angle of the light source and Δ is the opening angle of the diffuser (all referred to FWHM) [24]. α is not defined in the simulation, as the light hits the diffuser in random angles and on random points. Δ is set to 80°, as this is the maximum opening angle offered by the Luminit diffusers. Since the LSD is employed in special technical applications, its behavior for different radiation is largely measured.

On the surface, there are many randomly arranged tiny irregularities that work like slits or small lenses. Hence, if the LSD is illuminated diagonally, the beam is scattered within a cone, whose axis lies in the direction of the beam. For higher incidence angles with respect to the normal of the diffuser, the shape of the scattered light cone compresses in the direction that is not parallel to the diffuser [4].

Thus, a single photon scatters in this simulation in a random direction within a cone, whose opening angle is equal to the angle of the diffuser. The cone axis points in the same direction as the original direction of the photon. The deformation at higher incident angles is not considered.

3.4.2. Standard diffuser

The second type combines a whole bunch of actual diffusers, whose exact properties are not measured. For example, one of them is made by a thin layer of sintered polytetrafluoroethylene (PTFE). A rough consideration of samples showed, that these diffusers let a part of the light pass almost unimpeded, while the other part is scattered close to the ideal diffuser. The fraction of light that passes depends on the kind and thickness of the material.

This diffuser is partly implemented as an ideal diffuser and partly as a holographic diffuser with a small angle, to simulate the part of passing light. The opening angle approximates a Gaussian blur of the passing light. Since the exact properties of the different diffusers are not known, they were roughly estimated with a bunch of samples. The scattering part is chosen to be 70%, while 30% of the photons smear the direction within a cone with an opening angle of 10°. In this way, the general impact of this kind of diffuser and its parameters can be evaluated but one has to keep in mind, that the properties are not exactly known for these diffusers.

3.5. Generating random numbers

For the generation of the frequently needed random numbers the CERN ROOT number generator class "TRandom3" is used. This generator produces pseudo-random numbers with an algorithm based on [26]. Details can be looked up at the ROOT documentation [8] and the TRandom3 Class Reference [40].

ROOT provides an own function for vectors pointing uniformly distributed on a surface of a sphere that is used for the scattering on the walls and the ideal diffuser.

Furthermore, ROOT has a function for Gaussian distributed random numbers. Together with a uniformly distributed angle between 0 and 2π, this function is used for the reflection with a Gaussian blur.

3.5.1. Random positions uniformly distributed in a circle

In order to get a perfectly homogeneous hit distribution for comparison, it is needed to generate random positions that are uniformly distributed within a circle with radius R. While there are many ways to achieve this, the most common method is used in here and introduced in the following.

It is not enough to generate an angle ϕ and a radius r, that are uniformly distributed, since the circumference for circles nearer to the center is smaller. Hence, the same amount of positions is located in a smaller area and is therefore denser distributed [42].

To solve this problem, the radius r in the first method is calculated by

$$r = R\sqrt{a}, \tag{3.14}$$

where a is a random number uniformly distributed in the interval [0,1]. Furthermore, the angle ϕ is generated uniformly in the interval $[0,2\pi]$. The coordinates of the point then are

$$x = r \sin\phi, \tag{3.15}$$

$$y = r \cos\phi. \tag{3.16}$$

The distribution of 10^8 numbers that are generated in this way for a circle with radius 250 is shown in figure 3.5a.

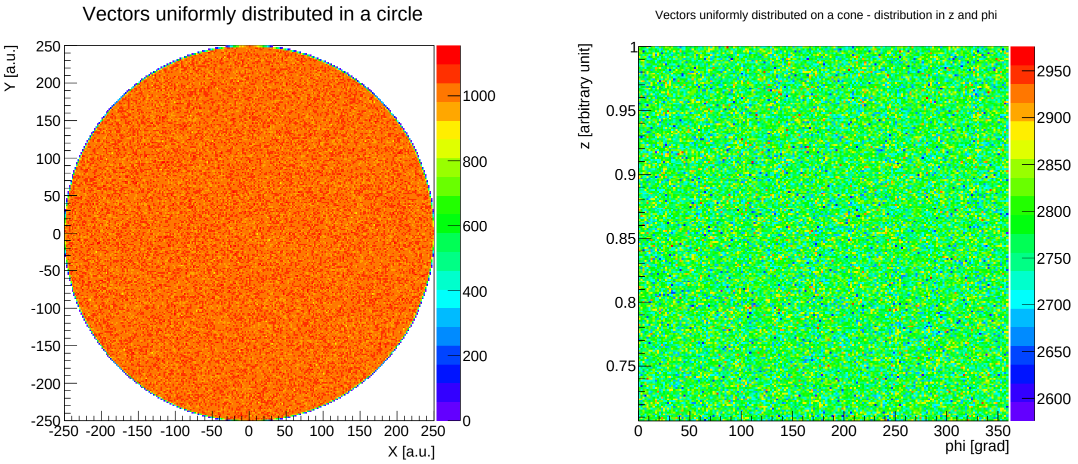

(a) xy-distribution for tuples that are uniformly distributed in a circle.

(b) Distribution of the z and ϕ value for vectors that are uniformly distributed in a cone.

Figure 3.5.: Distribution of 10^8 random vectors generated with the methods in section 3.5.1 and section 3.5.2, respectively.

3.5.2. Random numbers uniformly distributed in a cone

The generation of uniformly distributed vectors in a cone is slightly more difficult as ROOT does not provide a special function for these. The following method is used for the light source and the diffusers. If the cone axis is not equal to the global z axis (the z axis of the tube), the vector is generated in the coordinate system of the cone and will be transformed in the global system with the transformation matrix in section 3.6.1.

Let α be the opening angle of the cone. The z component of the vector can be directly obtained by sampling a number uniformly in the interval

$$z \in \left[\cos\left(\frac{\alpha}{2}\right), 1\right], \tag{3.17}$$

as two spherical segments have the same surface area (without the covers), if their height is the same, no matter where they were cut out of the sphere. The derivation can be found in appendix A.2. The polar angle θ now is

$$\theta = \arccos z. \tag{3.18}$$

Furthermore, φ, the azimuthal angle, is picked from the interval

$$\varphi \in [0, 2\pi]. \tag{3.19}$$

Thus, the x and y component are

$$x = \sin\theta \cdot \cos\varphi \tag{3.20}$$

$$y = \sin\theta \cdot \sin\varphi. \tag{3.21}$$

The vector (x, y, z) is uniformly distributed in a cone with an opening angle of α as shown in figure 3.5b. This plot shows the distribution of the z and ϕ value for 10^8 vectors that are generated with the above method for an opening angle of 45°. The method is based on [5].

3.6. Transformations

The direction vector of the photon often is calculated in a local coordinate system, due to simplification. Therefore the vector has to be transformed in the global coordinate system, where the z axis is defined by the symmetry axis of the tube.

For a rotation around the x, y or z axis the corresponding matrices are the Cartesian rotation matrices [20]

$$R_x(\alpha) = \begin{pmatrix} 1 & 0 & 0 \\ 0 & \cos\alpha & -\sin\alpha \\ 0 & \sin\alpha & \cos\alpha \end{pmatrix}, \tag{3.22}$$

$$R_y(\alpha) = \begin{pmatrix} \cos\alpha & 0 & -\sin\alpha \\ 0 & 1 & 0 \\ \sin\alpha & 0 & \cos\alpha \end{pmatrix} \tag{3.23}$$

$$\text{and} \quad R_z(\alpha) = \begin{pmatrix} \cos\alpha & -\sin\alpha & 0 \\ \sin\alpha & \cos\alpha & 0 \\ 0 & 0 & 1 \end{pmatrix}. \tag{3.24}$$

The rotated vector $\vec{a}_{\text{rotated}}$ for a rotation around the e_i axis by the angle α is

$$\vec{a}_{\text{rotated}} = R_\alpha(e_i) \cdot \vec{a}, \tag{3.25}$$

where $\vec{a}$ is the original vector in the local coordinate system. The rotation is counter-clockwise. For a clockwise rotation the sign of α changes.

In general, the rotation axis does not equal one of the coordinate axes. In this case several rotations around different axes have to be combined in a way that is described in the following.

3.6.1. Transformation matrix

The rotation matrix R_r around an arbitrary axis is more difficult but can be determined by the matrices above and an orthonormal basis (ONB) of the system.

Firstly, we want to calculate an ONB. Besides $\hat{r}$, our first vector in the ONB, we take

$$\hat{s} = \frac{\hat{r} \times \hat{e}_x}{\|\hat{r} \times \hat{e}_x\|} \tag{3.26}$$

or, if $\hat{e}_x$ is orthogonal to $\hat{r}$, then

$$\hat{s} = \frac{\hat{r} \times \hat{e}_y}{\|\hat{r} \times \hat{e}_y\|}. \tag{3.27}$$

If $\hat{s}$ and $\hat{e}_x$ are orthogonal too, then $\hat{s}$ equals $\hat{e}_z$ and $R_z(\alpha)$ is the rotation matrix. And as a third basis vector we choose

$$\hat{t} = \frac{\hat{r} \times \hat{s}}{\|\hat{r} \times \hat{s}\|}. \tag{3.28}$$

We now define the matrix R, by putting $\hat{r}$, $\hat{s}$ and $\hat{t}$ line by line as entries. Thus, R^{-1} is the matrix, where $\hat{r}$, $\hat{s}$ and $\hat{t}$ are put in column by column. Finally, the rotation matrix $R_r(\alpha)$ for a rotation around $\hat{r}$ by the angle α is given by

$$R_r(\alpha) = R^{-1} \cdot R_x(\alpha) \cdot R = \begin{pmatrix} tx^2 + c & txy - sz & txz + sy \\ txy + sz & ty^2 + c & tyz - sx \\ txz - sy & tyz + sx & tz^2 + c \end{pmatrix}, \tag{3.29}$$

where $t = 1 - \cos\alpha$, $c = \cos\alpha$ and $s = \sin\alpha$ [39].

In the context of a tilted cone, the rotation angle α is the angle between the cone's axis $\vec{c}$ and one of the Cartesian axes. The rotation axis $\hat{r}$ then is the normalized cross product of the cone's axis and the Cartesian axis, e.g. the x axis:

$$\theta = \arccos\left(\frac{\langle \vec{c}, \hat{e}_x \rangle}{\|\vec{c}\| \cdot \|\hat{e}_x\|}\right) \tag{3.30}$$

$$r = \frac{\vec{c} \times \hat{e}_x}{\|\vec{c} \times \hat{e}_x\|}. \tag{3.31}$$

3.7. ROOT and reasons for the exclusion of Geant4

ROOT is an object-oriented software package and library, which is based on C++. It is developed at the CERN for data processing and analysis for particle physics but is used in other fields such as data mining, too [8]. In this work, ROOT version 5.34 is used.

The Geant4 simulation platform, which is also developed at the CERN, is not used in the simulation. Geant4 is an object-oriented C++ based software to simulate the transition of particles in matter. It is preferably applied in high energy physics and nuclear experiments and medical, accelerator and space physics studies [1]. In this simulation it could have been used to simulate every photon as an actual quantum mechanical particle that correctly interacts with matter, i.e. air, the wall of the tube and the PMT, in the setup.

Instead, simple geometrical optics are used and implemented. Besides the effort that has to be put in to understand and implement the Geant4 platform correctly for the test facility, the computational effort to simulate a huge amount ($\gtrsim 10^7$) of photons will increase enormously. Furthermore, the simple geometrical assumptions are sufficient in the context of this work due to the macroscopic application. This allows to simulate a high amount of different scenarios relatively precisely in the time, that is needed to accurately simulate a single scenario with Geant4.

4. Structure of the simulation and reliability tests

This chapter introduces the structure of the simulation (section 4.1) and explains key methods (sections 4.1.1 and 4.1.2). Furthermore, issues, that could appear due to the structure and assumptions, and the implemented solutions for these are discussed. Last but not least, the plots that are used to visualize the results are explained (section 4.2) and first partially unexpected results of the simulation are shown and their plausibility are validated in section 4.3.

4.1. Structure of the simulation

The simulation calculates the path of single photons in the test facility, which is an idealized assumption striven for the real experiment but cannot always be achieved. With the statistics of many simulated photons, this results in an illumination distribution on the PMT surface. This distribution depends on the setup of different parameters in the tube. The goal is to find the best setup in the tube. To visualize the results, all relevant values, such as the position of the hit, the incidence angle and the running time of the photons are saved and their frequency of occurrence is plotted.

The path of a photon between two points of interaction is considered a straight line g, which is characterized by the current direction $\vec{d}$ and position $\vec{s}$ of the photon:

$$g : \vec{r} = \vec{s} + t \cdot \vec{d}, \tag{4.1}$$

with t being a real variable. The sign of the direction is not important in most cases as the relevant method chooses the next way point of the photon's path out of the two intersection points of a straight line with a cylinder or sphere according to the current position (see section 4.1.1). For cases, where the sign matters, it is specified accordingly.

After a photon is generated as described in section 3.3.5 the next way point is calculated by the method discussed in section 4.1.1. A second method, which is introduced in section 4.1.2, then generates the new direction. This process is within a loop as long as the photon is not detected by the PMT or absorbed. Then, a new photon can be generated until the total number of photons is reached.

4.1.1. Calculating the next point of interaction

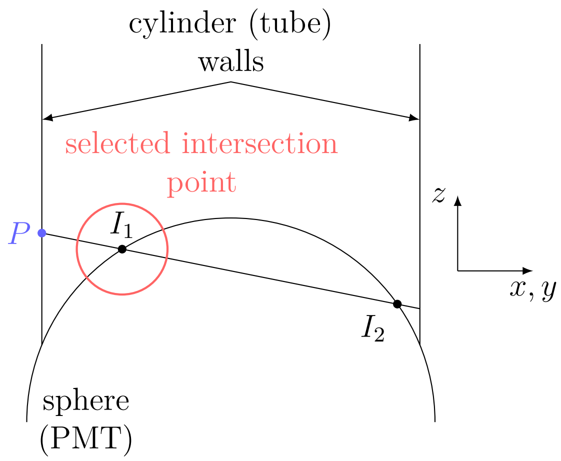

Figure 4.1.: Selection of the sphere line intersection point. I_1 is located closer to the current position P of the photon than I_2 and therefore chosen as the next intersection point.

The photon can either interact with the cylinder or the PMT which is considered a sphere in the simulation.

At first, it is checked, whether the photon's path crosses the bulb of the PMT. Therefore, the minimal distance d between the PMT center $\vec{p}_{\text{center}}$ and the straight line of the photon (equation (4.1)) is calculated by

$$d = \frac{\|(\vec{p}_{\text{center}} - \vec{s}) \times \vec{d}\,\|}{\|\vec{d}\,\|}. \tag{4.2}$$

This formula is derived in appendix A.5.

If the distance is lower than the radius of the PMT, the two interaction points of a straight line with the PMT sphere are calculated by

$$\begin{pmatrix} x \\ y \\ z \end{pmatrix} = \begin{pmatrix} s_x \\ s_y \\ s_z \end{pmatrix} + t_{1,2} \cdot \begin{pmatrix} d_x \\ d_y \\ d_z \end{pmatrix}, \tag{4.3}$$

where $\vec{r} = (x, y, z)$ is the intersection point, $\vec{s} = (s_x, s_y, s_z)$ is the current position and $\vec{d} = (d_x, d_y, d_z)$ is the direction of the photon,

$$t_{1,2} = \frac{-b \pm \sqrt{b^2 - 4ac}}{2a} \tag{4.4}$$

and

$$\begin{aligned} a &= \|\vec{d}\| \\ b &= 2 \cdot \langle \vec{d}, \vec{s} - \vec{p}_{\text{center}} \rangle \\ c &= \|\vec{s} - \vec{p}_{\text{center}}\| - R^2. \end{aligned} \tag{4.5}$$

Now, the intersection point lying closer to the photon's current position is chosen since this is the point which is hit first. This is visualized in figure 4.1. Principally, this intersection point can be located on the sphere on a point that cannot be reached, e.g. if the intersection point is located outside of the cylindrical tube.

In this case, and if the minimal distance to the PMT center is higher than the radius of the PMT, the intersection points of the photon's path and the cylindrical tube are determined by equation (4.3). In this case, $t_{1,2}$ is the same as in (4.4) but

$$\begin{aligned} a &= d_x^2 + d_y^2 \\ b &= 2(d_x s_x + d_y s_y) \\ c &= s_x^2 + s_x^2 - R^2. \end{aligned} \tag{4.6}$$

Or, if the z value in equation (4.3) does not satisfy

$$0 \leq z \leq h, \tag{4.7}$$

where h is the height of the cylinder, the corresponding t_i is set to

$$t_i = \frac{z_{\text{cover}} - s_z}{d_z}, \tag{4.8}$$

where $z_{\text{cover}} = 0$ or $z_{\text{cover}} = h$, respectively. One of the intersection points equals to the current position of the photon. Therefore, the second intersection point is chosen as the next way point. There is one exception which is discussed below. Due to `double` precision and rounding errors, the current position does not exactly equal to one of the calculated intersection points and thus the intersection point that is further away from the current position is selected. The selection is visualized in figure 4.2.

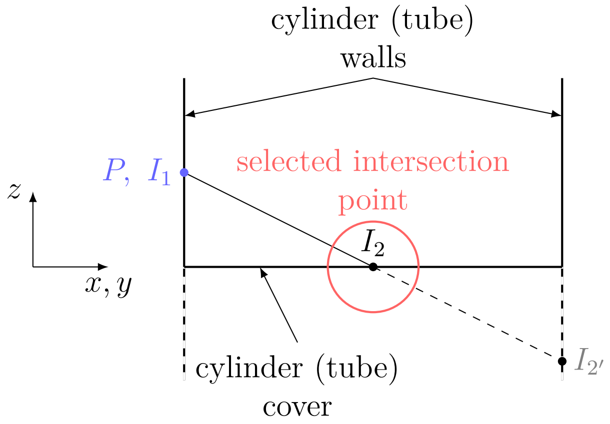

Figure 4.2.: Selection of the cylinder line intersection point. I_1 is the photon's current position P of the photon and can therefore be excluded as next way point. I_2' is located outside of the cylinder and hence it is replaced by I_2 on the cover, which is then chosen since it is further away from the current position P.

If the photon is reflected on the PMT surface, the sign of the direction vector is ensured to be correct. In this case, the intersection point which belongs to the positive t value is chosen as the next way point.

Finally, the current position is overwritten by the determined next position and the function returns whether the new position is on the PMT, the walls of the cylinder, the covers or the diffuser, if there is a diffuser included in the scenario.

4.1.2. Calculate the next direction vector

This method calculates the next direction vector $\vec{d}$ by performing a physical process based on the return of the method described in the previous section 4.1.1. Furthermore, this function registers PMT hits and fills the plots with the position on the PMT, the incidence angle and the running time of the photon. If more than one process is possible, it is chosen by comparing a random number to the variables that saves the ratio of the different process types.

There are two possible processes on the PMT surface:

- reflection (see section 3.3.4)
- actual hit

If the PMT is actually hit, which means the photon hits the photocathode, the histograms are filled with the relevant values as mentioned above and the photon is absorbed.

Choosing the process on the walls is a bit more complicated since it is composed of different material types. There are three regions in the most scenarios:

- 20mm absorbing material
- a definite amount of reflective material (Tyvek in most cases): see section 3.3
- rest is absorbing.

According to the position on the tube, the type of interaction with the walls is chosen.

If there is a diffuser in the scenario and it is hit, the direction is calculated according to the type of diffuser that is used. The different types are described in section 3.4.

As mentioned before, the sign of the direction is only guaranteed to be correct in two cases, since the direction information is possibly lost in the calculation process of the method in section 4.1.1. This also means that a vector pointing into the wall is treated as a vector which points into the opposite direction out of the wall. Therefore additional checks are needed to assure that the assumptions for the reflection and scattering are implemented correctly. This is negligible for the ideal scattering, since the vectors are distributed isotropic.

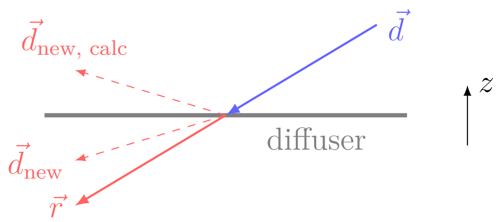

Figure 4.3.: If the calculated new direction vector $\vec{d}_{\text{new, calc}}$ points on the wrong side of the diffuser, the sign of the z component is changed to become $\vec{d}_{\text{new}}$.

However, there are some problems that can occur in this context. For the diffusers that smear the direction (sections 3.4.1 and 3.4.2), the randomly generated direction vector possibly points on the wrong side of the diffuser, which can be considered as a reflection on the surface without obeying law of reflection (section 3.3.1). On one hand, reflection can appear on the surface of the diffuser but is not considered in the simulation. On the other hand, high reflection angles are strongly preferred in a way that this assumption does not describe the physics in a good way. Hence, an alternative method to solve this issue is needed.

In this method the sign of the z component of the reflection vector is changed. Thus, the cone is wider in the direction parallel to the diffuser than in the other direction. Actually, the cone is compressed uniformly (see [4] and section 3.4.1). As this method describes a deformation for higher angles of the cone it is used in the simulation, even though the description does not fit perfectly. The method is sketched in figure 4.3.

For the Gaussian reflection, it is not enough to simply check the sign of a component, as the plane of reflection does not necessarily match with a plane that is perpendicular to x or y axis. Instead, the vector $\vec{d}$ points into the wall, if the scalar product of the normal $\hat{n}$ of the plane of reflection and the new direction vector is less than 0

$$\left\langle \vec{d}, \hat{n} \right\rangle < 0. \tag{4.9}$$

In this case the direction vector is set to be the vector of perfect reflection. Alternatively, the photon can be absorbed. Both variants are better than keeping the direction pointing into the wall, since this means that a fraction of the photons are reflected back in the direction where they came from as sketched in figure 4.4.

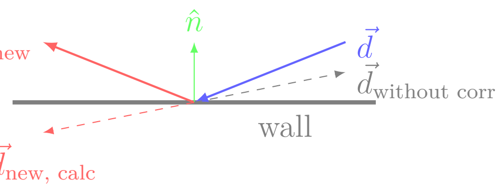

Figure 4.4.: If the calculated new direction vector $\vec{d}_{\text{new, calc}}$ points into the wall, it is treated like $\vec{d}_{\text{without corr}}$, which points in the wrong direction. Instead, $\vec{r}$ is selected as $\vec{d}_{\text{new}}$.

4.2. Explanation of the plots

A perfectly homogeneous hit distribution (PHHD) in the context of the simulation means that every point is hit statistically equally in the projection of the PMT surface on the xy plane. Therefore, a source that emits photons uniformly distributed on the upper cover of the PMT and parallel to the z axis is used as a reference. The appropriate hit distribution is shown in figure 4.5a. The PHHD does not imply a homogeneous distribution of every point of the photosensitive layer. Instead the illumination decreases outwardly if normalized on the surface of the PMT (see figure 4.5e). As the test facility only uses a single light source, a homogeneous illumination of every point cannot be

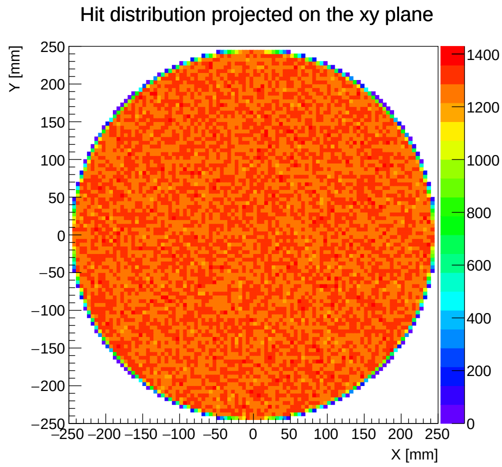

(a) *xy*-projection

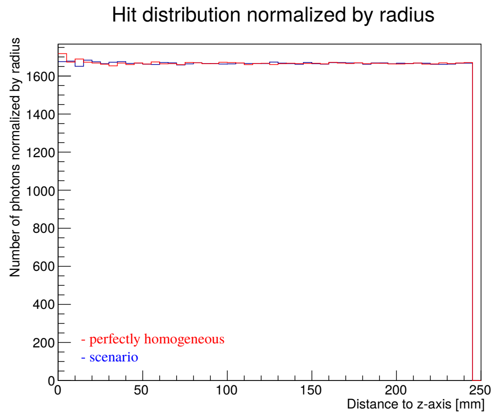

(b) Number of photons in a certain distance to z axis normalized by the radius of the corresponding ring.

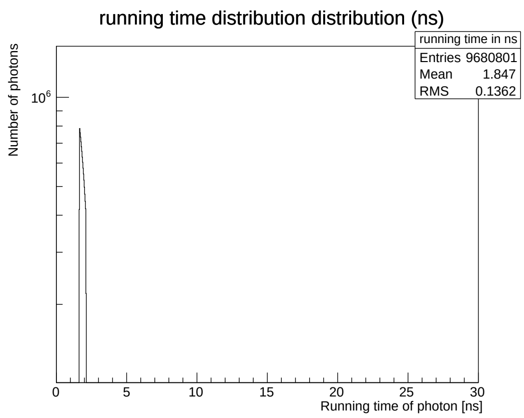

(c) Running time distribution.

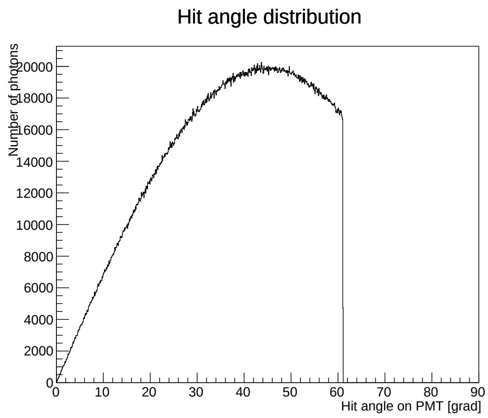

(d) Hitangle distribution.

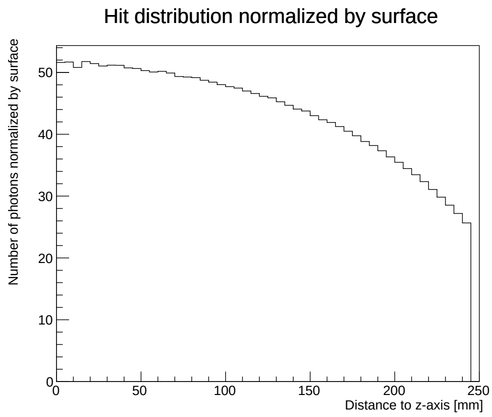

(e) Hit distribution normalized on surface of the PMT.

Figure 4.5.: Different plots that are used in this work, here an example of a perfectly homogeneous hit distribution.

achieved. Thus, the PHHD is a suitable definition for the test facility but central points are weighted more than the edge which may causes a higher systematic error in the average PDE and QE, respectively.

To visualize the results, mainly four different plots are used. In this section these are explained with the perfectly homogeneous hit distribution as an example. The first and probably most vivid plot 4.5a shows the 2D projection of the hit distribution on the PMT on the xy plane. This gives a direct visual feedback of the homogeneity.

This plot is not suitable for a quantitative evaluation regarding the deviation from the perfectly homogeneous hit distribution PHHD. For this, the number of hits in a certain distance from the z axis, normalized on the circumference (actually normalized on the radius, difference is a factor 2π) of the corresponding circle, is plotted in the second plot 4.5b. For comparison, the perfectly homogeneous distribution is added in red, whereby both histograms are scaled on the same number of processes. As the perfectly homogeneous hit distribution is also simulated, it contains statistical fluctuations. For the deviation, the difference between the minimum and maximum in the illumination is divided by the average of the perfectly homogeneous distribution (~ 1675). The outermost bins are neglected since these bins also contain of points on the PMT, that are not photosensitive.

The third plot 4.5c shows the running time distribution of the photons for the scenario. In the interest of readability the number of photons on the y axis is plotted logarithmically. The variance of the running time is given by the root mean square (RMS) value x_{RMS}, which is defined by

$$x_{\mathrm{RMS}} = \sqrt{\frac{1}{N}\sum_{i=1}^{N}(\bar{x} - x_i)^2}, \tag{4.10}$$

where N is the number of values and x_i are the single values and $\bar{x}$ is the mean value.

The hit angle distribution is displayed in the fourth plot 4.5d. The angle refers to the normal of the PMT surface in the hit point. The third and fourth plot are only plotted if the additional information is needed.

4.3. Example hit distributions

In this section, three simple examples and their hit distributions are briefly discussed. The first one (section 4.3.1) has totally absorbing walls, while in the other two, the tube is covered with reflective material, one with mirroring (section 4.3.2) and the other one with perfectly scattering material obeying Lambert reflection (section 4.3.3). For all three examples, 10^7 photons are simulated.

4.3.1. Absorbing material on wall

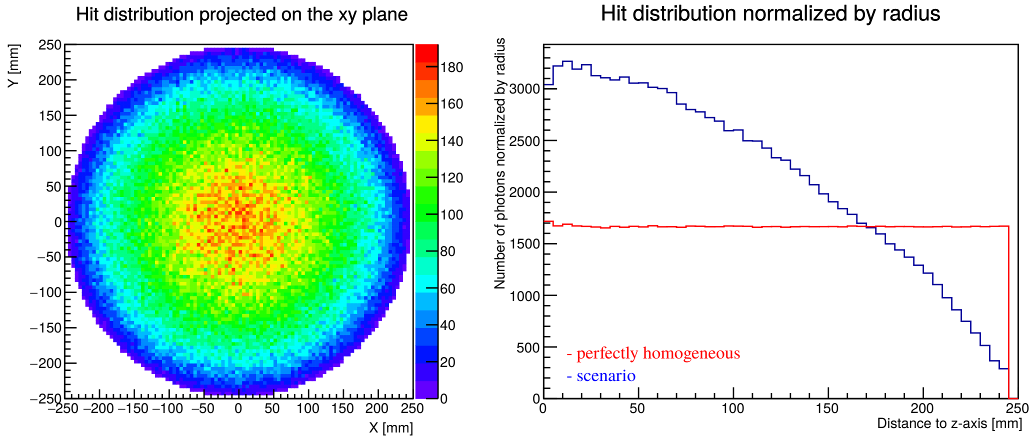

Figure 4.6.: Hit distribution for totally absorbing walls.

In this test, the walls of the tube are completely absorbing and the light source has an opening angle of 180°.

As only the photons hit the PMT's surface that also point directly onto it, this scenario can be used to test the validity of the implementation of the PMT hit detection in the simulation.

The shape of the hit distribution can be explained by the inverse-square law which states that the intensity of a point source is inversely proportional to the square of the distance to the source [16]. As the central points of the PMT surface are located closer to the light source than the points on the edge of the PMT, the illumination is much lower on the edge even though the light source is isotropic.

The illumination distribution is just as expected and the hit detection of the PMT can therefore be considered as correct.

4.3.2. Reflection

The totally reflecting walls produce a huge peak in the center of the PMT as figure 4.7a shows. This peak may appear counterintuitive at first sight but is indeed logical and will be explained in this section.

As the light source is punctual and exactly on the symmetry axis of the cylinder, the path of the photon will be completely in a plane, that consists of the z axis and the

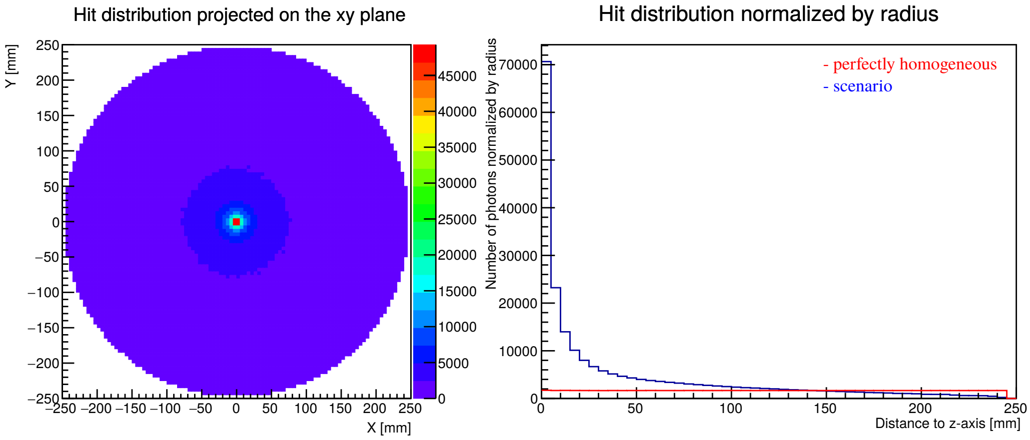

(a) Hit distribution for totally reflecting walls.

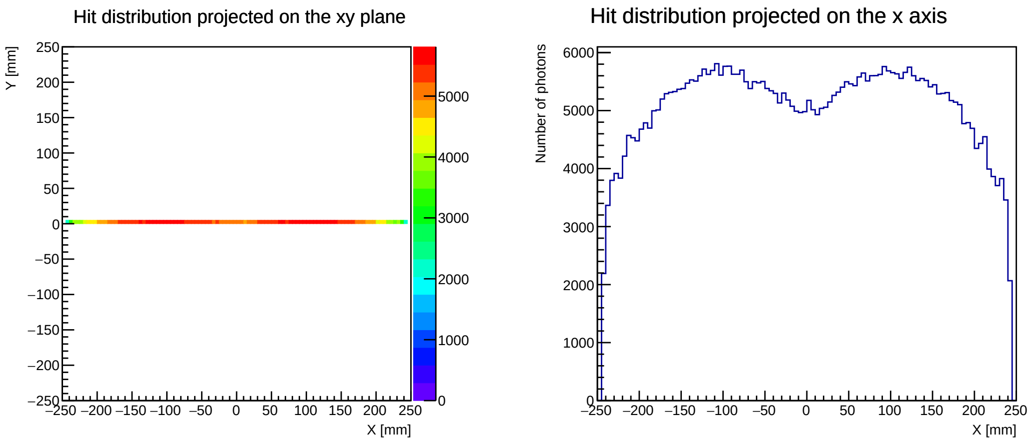

(b) Hit distribution for a light source that uniformly emits in xz plane. Since the normalization on the circumference does not make sense the second plot shows the projection of the hit distribution on the x axis. In this plot, only 10^6 photons are simulated.

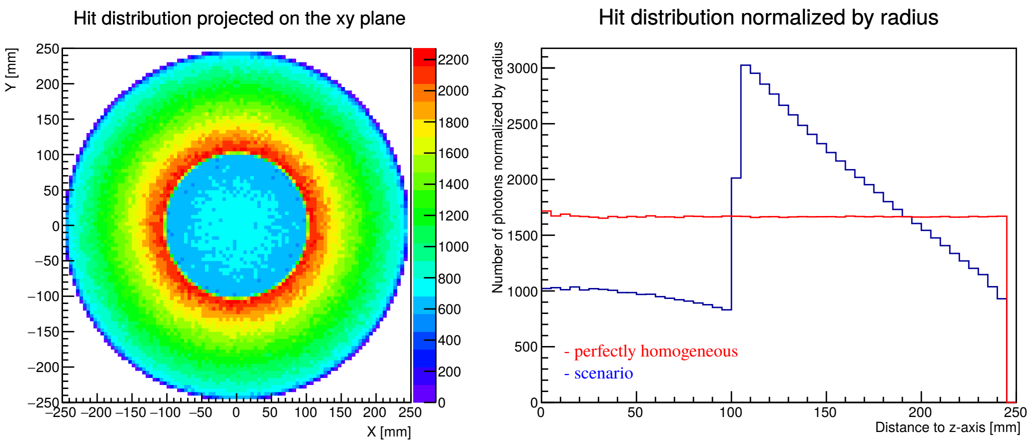

(c) Hit distribution for 300 mm reflective material on the walls and the rest absorbing.

Figure 4.7.: Different settings for the reflection to explain the peak.

connection vector between the z axis and the first point on the wall. Hence, the three dimensional path of a single photon can be described two dimensionally.

The hit distribution for a light source that emits isotropic only in the xz plane is shown in figure 4.7b. In this case, the center is not hit as much as the area between the center and the edge of the PMT. The only point all of these planes have in common is the center. Therefore, if the hit distribution in figure 4.7b is superimposed for every direction, the hits in the center add up to a huge peak, while the other points will only be hit for emission in one direction.

The center is hit mostly by photons that point directly from the source to the PMT center and the ones that are reflected only once in the middle between the top point of the PMT and the light source as visualized in figure 4.8.

To test this explanation, the length of the reflective material is reduced in a way that the relevant area on the walls is not reflective anymore. The result is shown in figure 4.7c, where the peak vanished as expected. Now, the center is only illuminated by photons that hit the PMT directly in this area. Assuming all points are equidistantly distributed along a straight line through the center, the lateral distance is increasing outwardly. Thus, the point density is higher in the central area of the PMT than on the edge. Hence, the number of hits per bin still increases steadily towards the center up to the point, where the reflective material is cut.

This argumentation also holds for Gaussian reflection in a similar but more complicated way. An example for this peak is shown in the results section in figure 5.1c for Tyvek reflection.

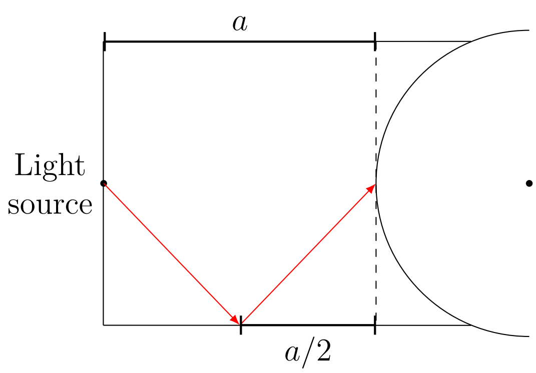

Figure 4.8.: Photons that reach the center of the PMT mostly follow the path showed in red.

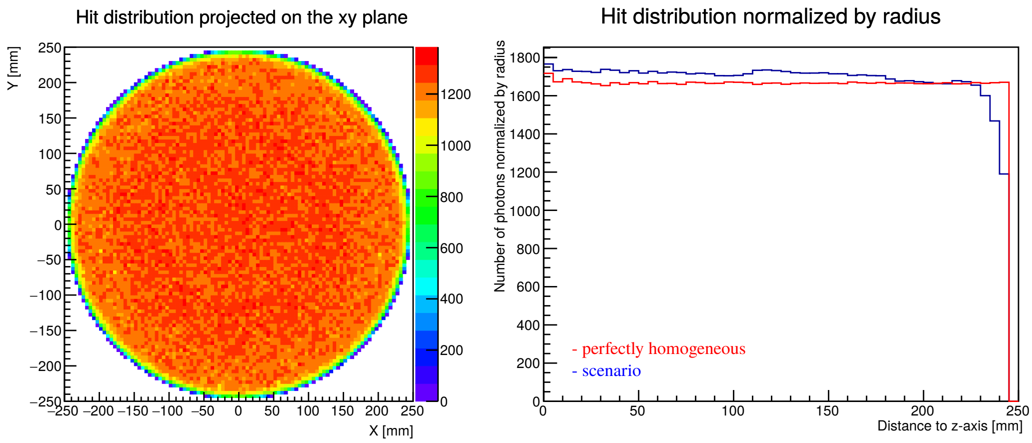

Figure 4.9.: Hit distribution for totally scattering walls.

4.3.3. Scattering

In this test, the walls are completely covered with ideally scattering material as described in section 3.3.2, with an exception for the 20 mm on the PMT side of the tube, which is absorbing as explained in section 3.1. The hit distribution, that is shown in figure 4.9 is almost homogeneous. Only the edge is illuminated a bit less than the center.

Although, the hit distribution is hard to predict, this result is plausible. The scattered photons have a random direction and therefore, every point of the photosensitive area should have a similar probability. However, due to the 20 mm absorption the edge of the photosensitive area is hit less.

5. Optimization of the setup

In this chapter, the impact of the single parameters for most realistic scenarios are discussed to find the best setup especially in terms of homogeneity, but in other aspects, too. There are two different main scenarios, one with a diffuser directly on the light source to have the source as isotropic as possible (section 5.1.1) and the other with an additional separate diffuser in the tube to add another source of scattering (section 5.1.2). For both scenarios, the best setup is found and compared with each other. Furthermore, the impact of small errors in the implementation (section 5.2) and the systematic error on the determination of the PDE for different possibly appearing PDE distributions of the PMT are tested in section 5.3. Based on these results the final setup is found (section 5.4). For all runs, 10^7 photons are simulated except of something different is stated.

5.1. Scenarios

The main task is to establish the setup of material and diffusers in the tube that optimize the homogeneity in the hit distribution of the PMT while keeping the variance σ_t of the running time as low as possible at the same time. There are several parameters that have to be taken into account including the settings for the light source, the material composition on the walls and the settings for possibly used diffusers.

Firstly, totally reflecting material can be excluded, since in this scenario most of the photons are focused in the PMT center as described and explained in section 4.3.2. Thus, only absorbing or scattering material can be chosen for the walls.

The absorbing material is assumed as totally (100%) absorbing, which can not be reached by a real material but the reflective part is negligible.

Tyvek is used as the scattering material as its properties come closest to the Lambertian scattering and it provides a low absorption. Details about the material and how it is modeled in this simulation can be looked up in section 3.3.3.

There are two major scenarios that are optimized and compared to each other. Their individual advantages and disadvantages are discussed in the following sections.

5.1.1. Diffuser at light source

The first scenario provides a diffuser on the light source which makes the light as isotropic as possible. It is referred as the scenario without a (separate) diffuser, since the diffuser on the light source can be considered as a part of the light source. The walls are partly covered with absorbing material and Tyvek in a way that has to be determined in this section.

Starting from 200 mm, the Tyvek length is increased up to total covering of the walls (620 mm) in 100 mm steps typically to find the range of the best setup. The setup should provide stable results when varying the Tyvek length in the area of 10 to 20 mm around the best setup , since the length could vary in the real implementation as well and should show an almost identical hit distribution to assure comparability and consistency.

The results of the 200 mm, 300 mm and 400 mm setups are shown in figure 5.1. Additional setups can be found in appendix C. As mentioned before in section 4.2, the outermost bins are neglected in the determination of the deviation between the minimum and maximum illumination.

The 200 mm setup (figure 5.1a) has a high illumination in the center and the edge of the PMT. The low amount of Tyvek combined with the high percentage of reflected photons at high angles (section 3.3.3) leads to the ring on the edge while the photons that hit the PMT directly (hit distribution comparable to the one in section 4.3.1) cause the higher illumination in the center. The deviation between the maximum and minimum is above 25% which is too large for the actual implementation.

The 300 mm setup (figure 5.1b) has a ring of higher illumination with a radius around 100 mm to 175 mm. As a result, the deviation between the maximum and minimum of the illumination is between 10% and 15%, which is a bit above the 10% goal as mentioned in section 3.2.1. However, further optimizations showed that this is the overall best setup in this scenario and it is stable in the range of 280 mm to 320 mm, which can be found in the appendix C as well. Therefore, the impact of small deviations in the Tyvek length are negligible.

The 400 mm setup (figure 5.1c) has a high peak in the center of the PMT that is caused by the reflecting part of the Tyvek. Compared to the peak of only reflecting material (explained in section 4.3.2) this peak is broader, caused by the Gaussian blur

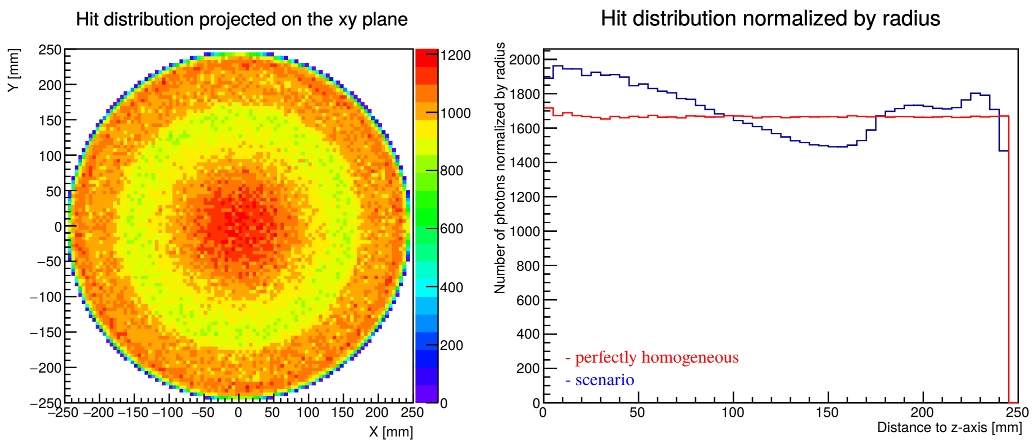

(a) 200 mm Tyvek

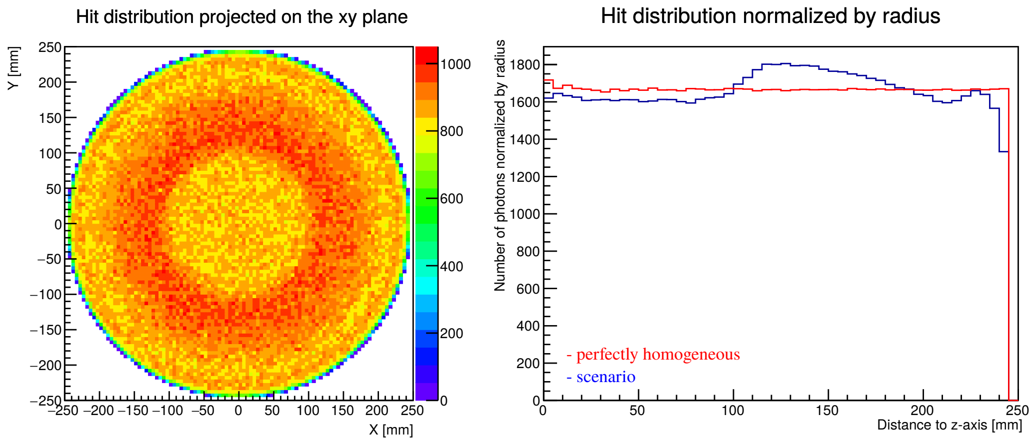

(b) 300 mm Tyvek

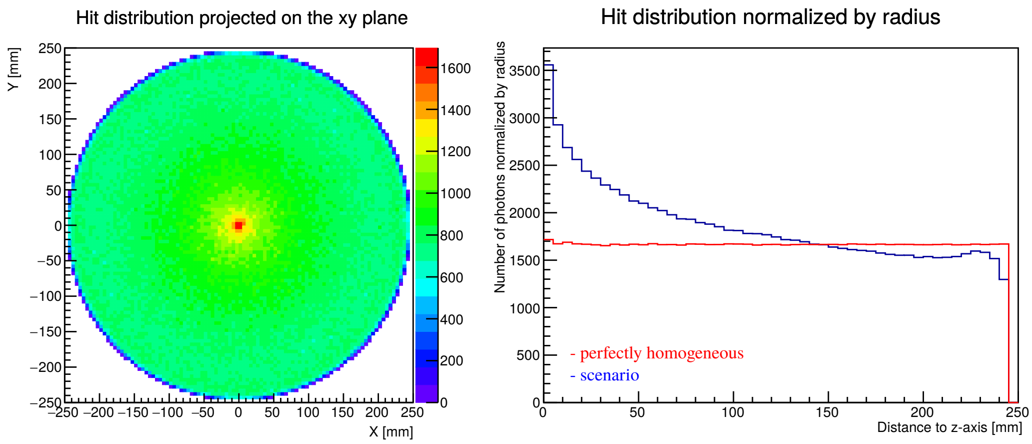

(c) 400 mm Tyvek

Figure 5.1.: Hit distributions for the scenario without a separate diffuser. Left: Hit distribution projected on the xy plane. Right: Number of hits in a certain distance from the z axis normalized by the radius/circumference of the ring.

of the reflection, and not as dominant, since the scattering produces an almost uniform hit distribution (section 4.3.3). In the two other scenarios this peak does not appear because the relevant part of the tube, that causes this peak, is not illuminated. This setup's hit distribution is inhomogeneous. Similar results are obtained by setups with higher Tyvek length.

5.1.2. Separate diffuser

The second scenario uses an additional diffuser that splits the tube into two parts perpendicularly to the tube's axis. This scenario is referred as the scenario with a (separate) diffuser. The purpose of a diffuser is to provide an additional source of scattering that prevents the photons from hitting the PMT directly. This should compensate anisotropies of the light source and its alignment and generally increase the homogeneity on the PMT's surface.

As can be seen in figure 5.2 all the different diffusers increase the homogeneity massively. The Tyvek length is 300 mm in each case, while the diffuser is placed in a distance of 385 mm of the light source. The position of the diffuser was determined by testing different positions. As expected, the ideal position depends on the Tyvek length and the diffuser should not be located too close to the PMT. For the 300 mm Tyvek length, the ideal distance is 385 mm.

The ideal diffuser (figure 5.2a) has two areas with a slightly higher illumination. The higher illumination on the center is caused by the short distance of the top of the PMT and the diffuser while at the same time more photons hit the center of the diffuser than the edge. The other peak on the edge is caused by the increased reflective part of Tyvek for higher incidence angles. The deviation between the maximum and minimum in the hit distribution is slightly below 10%.

The holographic diffuser almost reaches the perfectly homogeneous hit distribution (figure 5.2b). Only the edge has a minimally higher illumination that is again caused by the Tyvek reflection properties. Thus the deviation between the maximum and minimum is mostly below 4.5% without the peak on the edge. Including the edge leads to a deviation of 7.5% with it.

The standard diffuser with 70% ideal scattering and 30% photons that keep the direction within an opening angle of 10° has a homogeneous hit distribution, too (figure 5.2c). By a more detailed look the same pattern as for the 300 mm setup without a diffuser can be seen. This is caused by the photons that can pass the diffuser almost

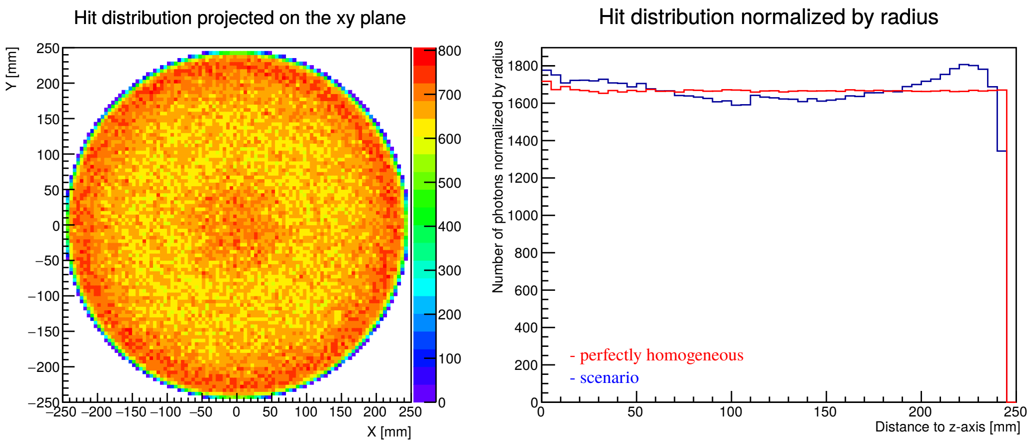

(a) Ideal Diffuser

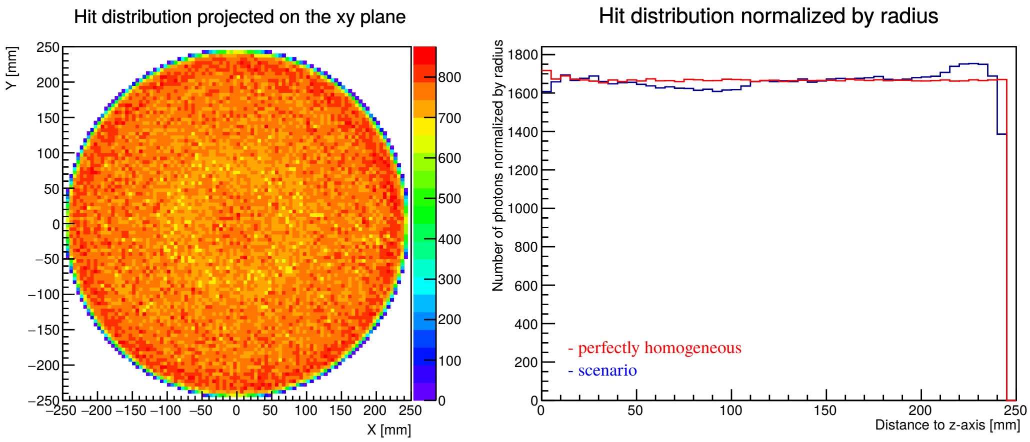

(b) Holographic Diffuser with 80° opening angle

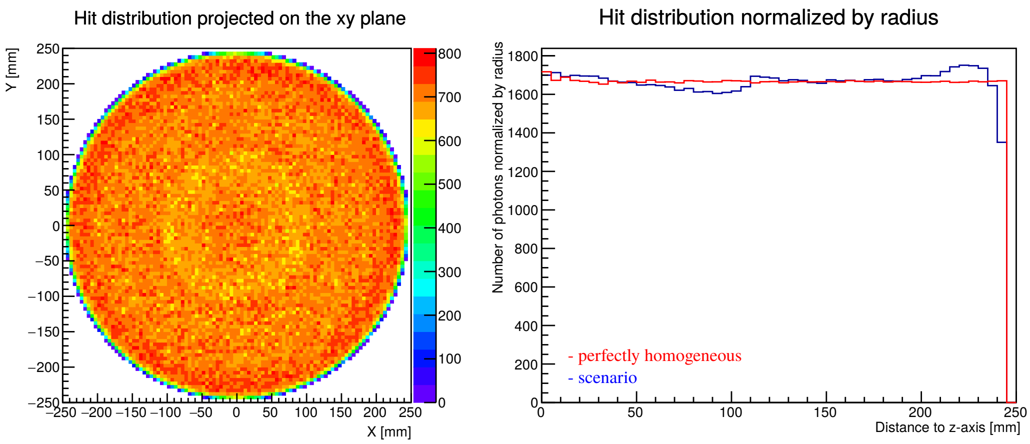

(c) Standard Diffuser with 70% scattering and 10° opening angle

Figure 5.2.: Hit distributions for the setup with a separate diffuser. Left: Hit distribution projected on the xy plane. Right: Number of hits in a certain distance from the z axis normalized by the radius/circumference of the ring.

unhindered. The deviation between the maximum and minimum in the illumination is about 9%.

As the holographic diffuser provides the best hit distribution and its properties are known better than for the standard diffuser, this setup can be considered as the best with a separate diffuser. Therefore it is compared to the best setup without the separate diffuser.

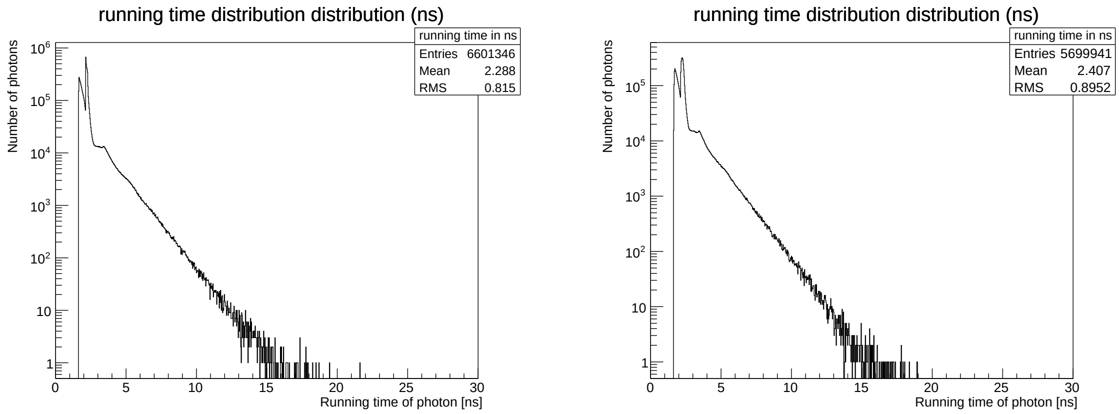

(a) Without separate diffuser

(b) With holographic diffuser

Figure 5.3.: Comparison of the running time for the best setup with and without a diffuser.

The running time of the photons is shown in figure (5.3) for the 300 mm setup and for the setup with the holographic diffuser. As expected, the running time is a bit higher for the setup with diffuser, but the difference is negligible. The first peak is caused by photons that directly hit the PMT, while photons that are reflected or scattered once produce the second peak. For the diffuser both peaks are more blurred as the diffuser creates another kink in the the photon's path. The variance is below the desired (see section 3.1.3) 1 ns for both setups.

The hit angle distribution (figure 5.4) is similar for both scenarios, even if it is a bit smoother for the setup with diffuser. High and low angles are very rare, while the range of 30° to 50° is the most common. Due to the higher reflection on the PMT surface for higher hit angles, the distribution is asymmetric.

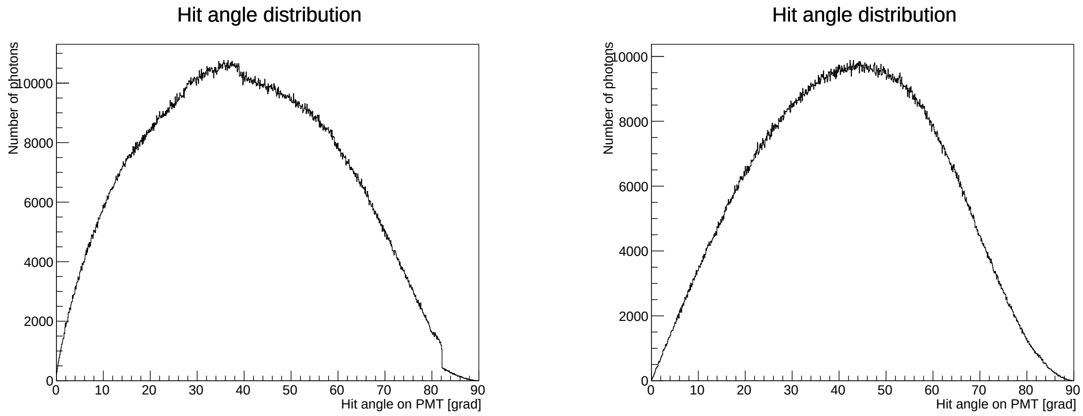

(a) Without separate diffuser

(b) With holographic diffuser

Figure 5.4.: Comparison of the angle distribution for the best setup with and without a diffuser. The hit angle is defined relative to the normal on the PMT surface in the hit point.

5.2. Impact of small errors in the implementation

This section discusses the impact of small inaccuracies in the implementation of the test facility by slightly changing some of the parameters in the simulation. Especially a tilt and shift of the light source is discussed as it is a possible error source.

The results of sections 5.1.2 and especially 5.1.1 imply, that small differences (mm to a few cm) in the length of the tube and of the Tyvek do not have a huge impact on the hit distribution. The diameter of the tube and the PMT radius are variable, too.

The impact of a tilt about 2° and 5° is shown in figure 5.5 for the 300 mm setup with and without a diffuser.

The impact of the 2° tilt is noticeable but negligible for both scenarios. Especially the diffuser eliminates the influence almost completely due to the additional source of scattering. The scenario without the diffuser lacks of this and is therefore more prone to the tilt. The hit distribution is still very similar to the one without the tilt and can be considered acceptable. As discussed in section 3.3.5, the 2° tilt can appear in the implementation.

If the light source is tilted in a 5° angle, the focus of the hit distribution is clearly shifted towards the positive x axis. Again, the diffuser compensates some of the inhomogeneities and was not affected as much as the setup without a diffuser. The 5° angle tilt is only used to test the impact of the tilt in a more extreme way since the 2° tilt lowered the homogeneity only slightly. Such a high angle should not appear in the actual implementation of the test facility.

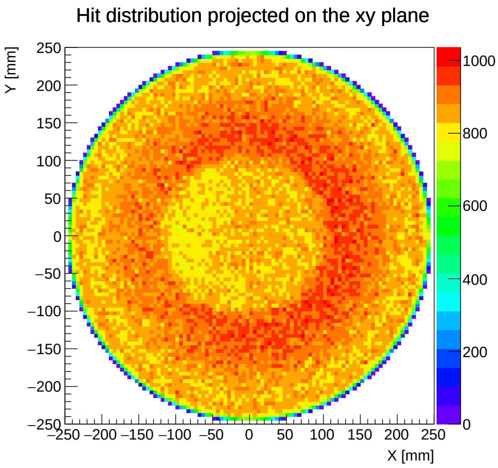

(a) Without separate diffuser, 2° tilt of light source

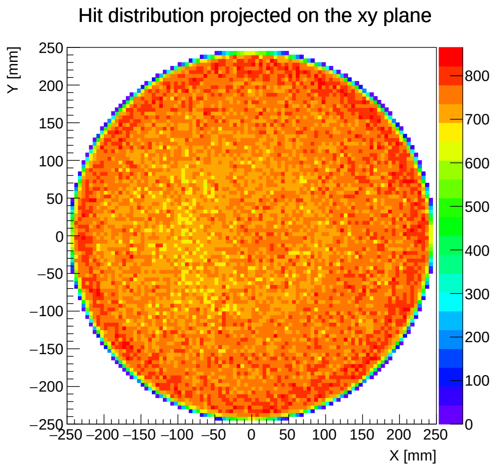

(b) With holographic diffuser, 2° tilt of light source

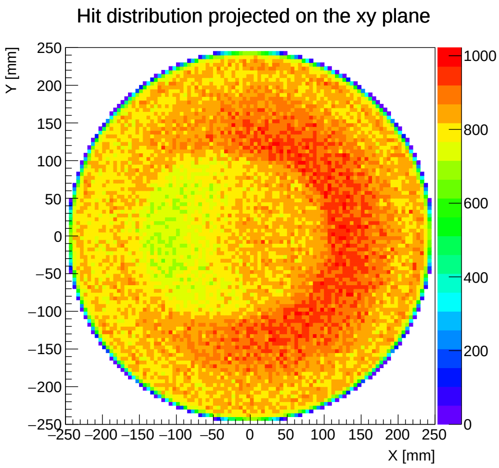

(c) Without a seperate diffuser, 5° tilt of light source

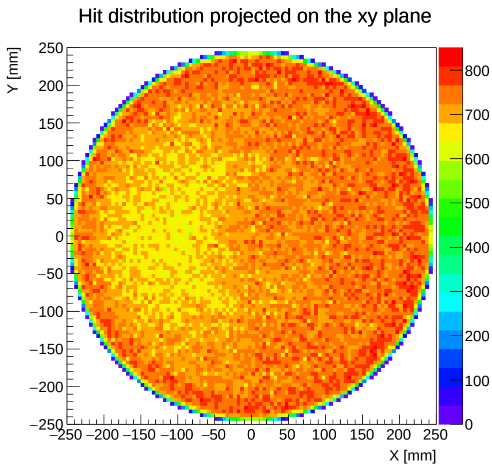

(d) With holographic diffuser, 5° tilt of light source

Figure 5.5.: Comparison of the hit distributions for the best setup with and without a diffuser, if the light source is tilted about 2° (above figures) and 5° (below figures).

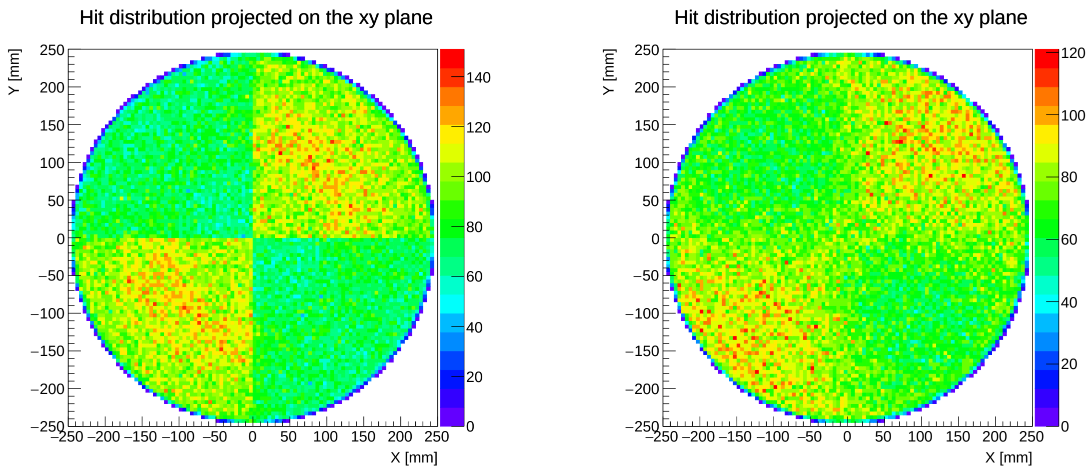

(a) Without diffuser

(b) With holographic diffuser

Figure 5.6.: Comparison of the hit distributions for the best setup with and without a diffuser, if the light source is (extremely) anisotropic.

Furthermore, the impacts of inhomogeneities of the light source are determined. The light source is divided in four quarters with two diagonally opposite quarters each having the same output (referred to as quarters light source). The deviation between the two parts is 25 % and is therefore an extreme example, which should clarify the impact. As shown in figure 5.6a, the inhomogeneity has a direct impact on the illumination of the PMT. In the direction of the quarters with a higher output, the illumination is much higher than in the other two quarters. The diffuser on the other hand (figure 5.6b) blurs the impact as expected. However, the inhomogeneities are still clearly visible. Therefore, the output of the light source has to be as isotropic as possible to avoid this huge source of errors from the beginning. As a solution, a diffuser is implemented directly on the light source. Then the output is scattered initially, while the implementation is less complicated than for the separate diffuser.

Besides the more homogeneous hit distribution, the diffuser also compensates small errors in the implementation. On the other hand, the diffuser is a source of errors itself. It is hard to attach and align the diffuser exactly within the tube. The impact of these inaccuracies cannot be simulated and is difficult to predict. As the setup without a separate diffuser falls back only slightly, none of the setups should be preferred.

5.3. Systematic errors on the photo detection efficiency

One important goal of the test facility is to measure the photo detection efficiency of the PMTs. Thus, the systematic errors on the photo detection efficiency is determined for the two best setups and the different PDE distributions as described in the following section 5.3.1.

5.3.1. PDE distributions on PMT

Six PDE distributions were defined in the simulation, that model different inhomogeneities that can appear for a real PMT. These distributions are explained in the following.

The first PDE distribution simply is homogeneous and like all of the PDE distributions it has an average PDE of $\oslash = 30\,\%$, as this is the goal for the actual PMTs. The xy projection is shown in figure 5.7a.

The second one (shown in figure 5.7b) adds single small deadspots on the surface, where the PDE is 0. Each of the three spots has a radius of 10 mm and their centers are located at the coordinates (50,0), (-150,150) and (0,-400), which refer to the position on the xy projection in mm (this type of coordinates is always used in the following).

The third and fourth PDE distribution (shown in figure 5.7c) divides the photosensitive area of the PMT in two parts with the same area on the spherical surface (not the projection on the xy plane). On of them has a constant PDE of $\xi = \oslash \pm \delta$, while the other part has $\xi = \oslash \mp \delta$. The first part is a combination of four spots at the coordinates $(\pm 245, 0)$ and $(0, \pm 245)$. The second part consists of the rest of the photosensitive area, which has the opposite sign for the deviation δ of the average PDE $\oslash$. It is $\delta = 7.5\,\%$ as an approximation for the maximum allowed deviation from the average PDE.

The fifth and sixth ones (shown in figure 5.7d) have two slim rings of same area on the spherical surface (not the projection on the xy plane), that are located next to each other. One of the rings has $\xi = \oslash + \delta$ and the other one $\xi = \oslash - \delta$. Again, the deviation is $\delta = 7.5\,\%$.

5.3.2. Results

Table 5.1 shows the conversion factors δ_{PDE} and measured average PDE for both scenarios and the relative deviation from the actual average PDE of 30%. The conversion factors are determined with equation (3.6) by taking the mean value of ten simulations with 10^6 photons.

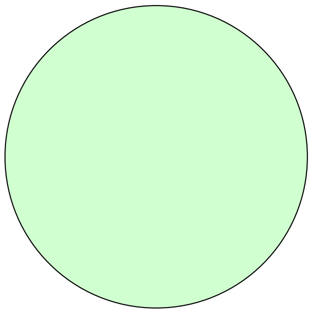

(a) Homogeneous PDE distribution with average PDE of 30%.

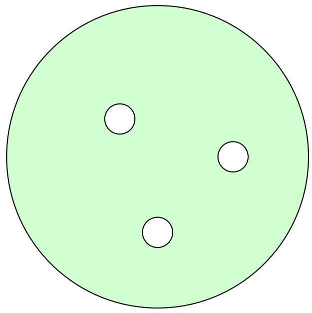

(b) Three small deadspots ($r = 10\,\mathrm{mm}$) with PDE = 0 at the coordinates (50,0), (-150,150) and (0,-400).

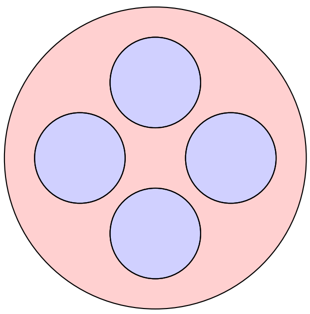

(c) Four spots with combined half of the photosensitive area with higher/lower PDE relative to the rest at the coordinates $(\pm 245, 0)$ and $(0, \pm 245)$.

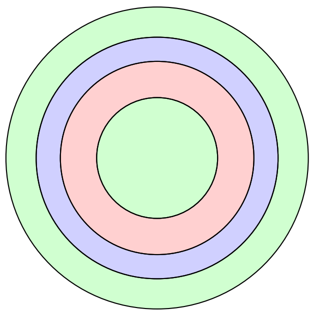

(d) Two rings with the same area and combined width of 50 mm, one with higher and the other with lower PDE.

Figure 5.7.: Sketches for different PDE distributions, projection of the spherical distribution on the xy plane and not to the scale. The coordinates refer to the position on the xy projection in mm.

The systematic error of the photo detection efficiency is very similar in both cases. The deviation between the measured average PDE and the actual average PDE is below 1% in both scenarios for all PDE distributions except the spots with higher or lower PDE, where it is about 5%. Although spots with higher/lower PDE are very probable to appear, these spots should be much smaller for a real PMT.

These results imply, that the homogeneity of the hit distribution only has a small impact on the systematic error of the PDE. However, if the inhomogeneities in the illumination coincide with the inhomogeneities of the PDE distribution of the PMT, these will be weighted more and the average PDE will have a higher systematic error.

The similar results for both scenarios with very different hit distributions suggest that the systematic error is dominated by the initial inhomogeneity in the definition of the PHHD (see section 4.2). Nevertheless, the average PDE can be measured fairly precisely for PMTs where the deviation of the PDE distribution from the homogeneous distribution is low. For a accurate calibration of the test facility with a high amount of different reference PMTs, the systematic error can be also reduced for the PMTs with a higher deviation.

Thus, the homogeneity is an important criterion but little inhomogeneities can be tolerated if the setup is better overall.

Table 5.1.: Conversion factor δ_{PDE} and measured average PDE $\overline{\xi}$ for each PDE distribution with the relative deviation from the actual average $\overline{\xi}_{\mathrm{actual}} = 0.30$ for the best setup with and without a separate diffuser.

PDE distributions	without diffuser, $\delta_{\mathrm{PDE}} = 1.51 \pm (0.1\%)$		with diffuser, $\delta_{\mathrm{PDE}} = 1.76 \pm (0.2\%)$	
	$\overline{\xi}_{\mathrm{measured}}$	rel. $\Delta\overline{\xi}_{\mathrm{measured}}$	$\overline{\xi}_{\mathrm{measured}}$	rel. $\Delta\overline{\xi}_{\mathrm{measured}}$
homogeneous	0.2998	-0.06%	0.3	$7.43 \cdot 10^{-4}$%
deadspots	0.2988	-0.39%	0.299	-0.34%
spots with higher PDE	0.2838	-5.39%	0.285	-5.0%
spots with lower PDE	0.3159	5.31%	0.315	5.0%
two rings, bad first	0.3015	0.48%	0.3018	0.61%
two rings, good first	0.2981	-0.65%	0.2983	-0.56%

5.4. Final setup

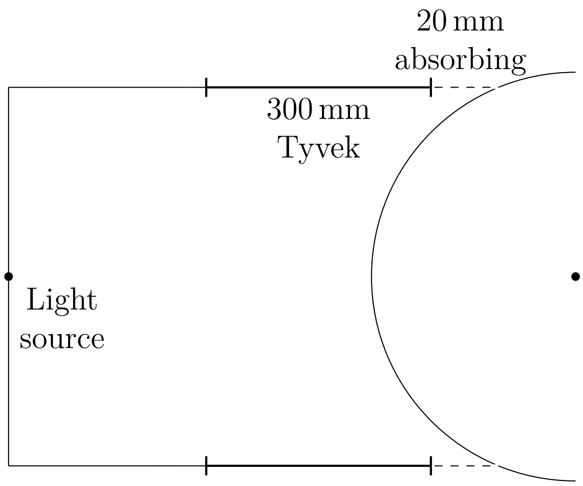

Figure 5.8.: Final setup of the test facility (not to scale) with 300 mm Tyvek and without a separate diffuser.

This section discusses the final setup for the actual implementation in the test facility.

The best results in terms of homogeneity and stability of the hit distribution are definitely provided by the setup with 300 mm Tyvek and the holographic diffuser. The result reaches, with a single exception on the edge, an almost perfectly homogeneous hit distribution and is not prone to errors in the implementation.

The deviation between the maximum and the minimum in the hit distribution takes values of maximum 7.5% but around 4.5% for the inner area of the photosensitive area. In comparison, the best setup without a separate diffuser comes along with a deviation between 10% and 15%.

Furthermore, errors in the implementation, such as a tilt of the light source, and an anisotropic light source have a direct impact on the hit distribution in the scenario without a diffuser, but are corrected partially by the diffuser. Small inhomogeneities of the output of the light source are corrected in both scenarios, since in the setup without a separate diffuser there is a small diffuser as part of the light source.

As stated in section 5.3, the systematic error of the photo detection efficiency is similar in both scenarios and does not depend on the homogeneity of the hit distribution as much as expected. The systematic error is dominated by the inhomogeneity of the PHHD relative to the actual perfectly homogeneous distribution which is normalized on the surface instead of the circumference. However, the systematic error is still very low for most of the PMTs.

This raises the question, whether the additional effort to implement the separate diffuser is necessary, especially, when the light source has a diffuser anyway. Despite providing very good results for the assumptions made in section 3.4.1, this scenario has some disadvantages to deal with. The assumptions in section 3.4 are based on the statements of the manufacturer of the holographic diffuser, Luminit, and are not confirmed independently. Moreover, the diffuser is an additional source of errors as its implementation in the tube is not easily done.

Since the budget for the test facility is very limited, an additional cost source is unwelcome. Especially the LSD of Luminit are costly due to their professional scope of application.

Parallel to this thesis, another simulation was implemented in the research group of the University of Tübingen by David-Samuel Blum. There, the 300 mm setup without a separate diffuser was independently confirmed as the best scenario, if the diffusers are not considered. The two 300 mm setups are compared in figure 5.9. The hit distribution has a similar shape in both simulations, although the inhomogeneities are more noticeable in the results of this simulation. This is caused by the different color code in the plots and the higher amount of bins and therefore higher fluctuations in this simulation.

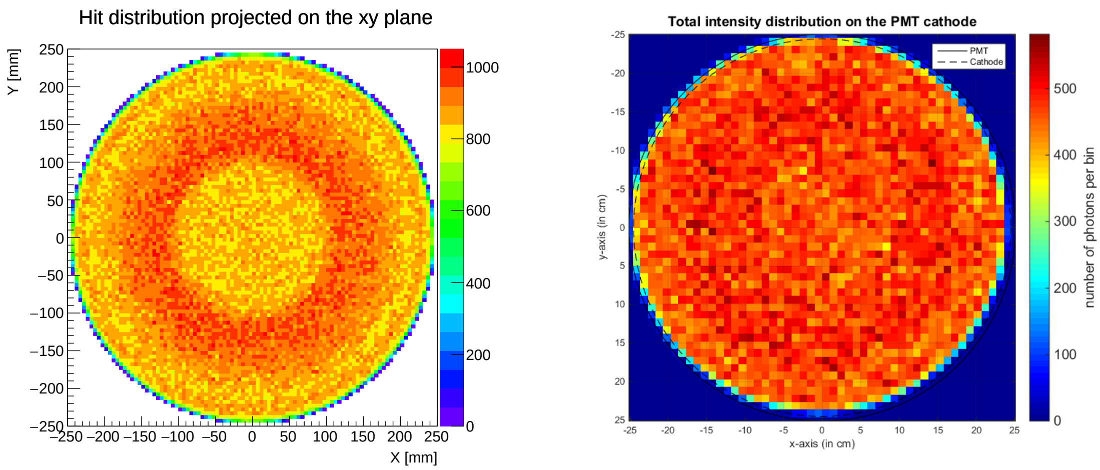

(a) Hamburg **(b)** Tübigen

Figure 5.9.: Comparison of the 300 mm setup without a diffuser of this simulation with the results of the Tübingen simulation [6].

As a result, the best scenario without a diffuser will be the final setup of the test facility described in section 5.1.1. This setup consists of a Tyvek stripe with the width of 300 mm and a diffuser implemented directly on the light source. The final setup is sketched in figure 5.8.

6. Conclusion and Outlook

Within the scope of this thesis, the lightfield of a test facility to characterize the JUNO PMTs was analyzed. The test facility consists of a single light source pointing onto the PMT while the whole implementation is bound by a cylindrical tube with the purpose of shaping the lightfield on the PMT. This test facility was simulated in several scenarios with and without a separate diffuser besides the one on the light source to find the best setup in the tube. The goal is to get an as homogeneous as possible hit distribution which causes a low systematic error in the determination of the average photo detection efficiency or photo detection efficiency, respectively. Furthermore, the impact of small inaccuracies in the implementation on the illumination of the PMT was tested. In particular, the influence of a tilt of the light source was determined.

This analysis resulted in two setups, one without and the other one with a diffuser, that were compared to each other. Both setups have a 300 mm stripe of Tyvek on the PMT end of the tube. The diffuser is located in a distance of 385 mm from the light source for the diffuser setup. In terms of the homogeneity of the illumination on the PMT, the diffuser setup definitely wins. With an exception on the edge, the deviation between the maximum and minimum illumination is at most 4% and increases on the edge to 7.5% (see section 5.1.2). For the setup without a separate diffuser this deviation is between 10% and 15% and thus slightly above the goal of 10% (see section 5.1.1). Moreover, the diffuser serves the purpose of reducing the impact of small errors in the implementation, even though the impact is small for both scenarios (section 5.2). At the same time, the diffuser is a source of errors itself as its implementation is not easy and prone to inaccuracies. Furthermore, the properties of the diffuser are not exactly known and only implemented idealized in the simulation.

The systematical error of the photo detection efficiency is below 1% except for extreme differences to the homogeneous PDE distribution and very similar for both scenarios (section 5.3). There are two things that can be concluded from the results. Firstly, the dominating inhomogeneity is not the one that is caused by the setup relative to the PHHD but the one that caused by the definition of the PHHD (see section 4.2) which results in a high systematical error for PMTs that are extremely different to the homogeneous PDE distribution. This can possibly be compensated by an outwardly increasing hit distribution. Secondly, the systematic error does not depend as much as expected on the homogeneity of the illumination. For most of the PMTs the systematic error is below 1% (without considering other aspects that influence the determination of the PDE). This and the implementation issues led to the decision to apply the 300 mm setup without the diffuser as the final setup in the actual test facility (see section 5.4).

Based on the results of the simulation the cardboard rolls are laminated with 300 mm Tyvek. The implementation of the first container will be finished and then the calibration process of the test facility will start soon. To do so, PMTs with known PDE (e.g. tested with the spatial resolved method introduced in section 3.2.1) are used to get the fraction of actually hitting photons, the conversion factor from section 3.2.2. Then, the PDE can be determined. Moreover, the reproducibility and consistence of the results of all tubes will be reviewed and, if necessary the setup has to be adjusted. Then the acceptance test can be started.

Later, the implementation of the calibration test has to be defined. While the simulation in this thesis is specialized on the acceptance test, the mandatory simulation for the calibration can be based on this thesis and its results, especially the ones for the diffuser can be of interest. For this, it is appropriate to make more detailed assumptions and define the lightfield exactly and close to the actual lightfield in the detector. As in the acceptance test, the simulation can be used to find a fitting setup while the actual implementation has to be calibrated and characterized experimentally.

A. Derivation of important formulas

A.1. Reflection formula

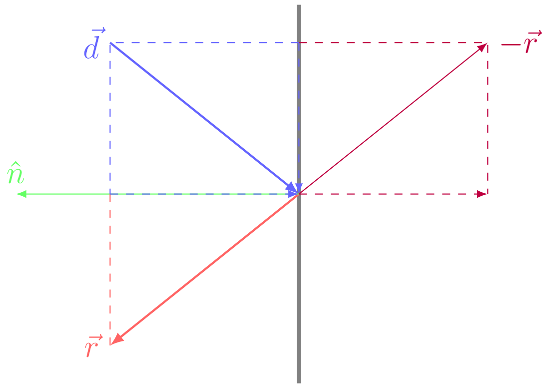

Figure A.1.: Reflection on a wall.

Let $\hat{n}$ be a normalized normal to the plane of reflection, $\vec{d}$ the incoming and $\vec{r}$ the reflection vector. Then, the projection of $\vec{d}$ on $\hat{n}$ is

$$\vec{a} = \left\langle \vec{d}, \hat{n} \right\rangle \hat{n} \tag{A.1}$$

and therefore

$$\vec{b} = \vec{d} - \left\langle \vec{d}, \hat{n} \right\rangle \hat{n} \tag{A.2}$$

the orthogonal projection, since $\vec{d}$ can be written as the orthogonal decomposition

$$\vec{d} = \vec{a} + \vec{b}. \tag{A.3}$$

As one can see in figure A.1, $-\vec{r}$ can be decomposed as

$$-\vec{r} = \vec{a} - \vec{b} \tag{A.4}$$

$$\Leftrightarrow \qquad \vec{r} = -\vec{a} + \vec{b}$$
$$= \vec{d} - \left\langle \vec{d}, \hat{n} \right\rangle \hat{n} - \left\langle \vec{d}, \hat{n} \right\rangle \hat{n}. \tag{A.5}$$

This leads to a simple formula for the reflection vector:

$$\vec{r} = \vec{d} - 2 \cdot \left\langle \vec{d}, \hat{n} \right\rangle \hat{n}. \tag{A.6}$$

A.2. Surface area of a spherical segment

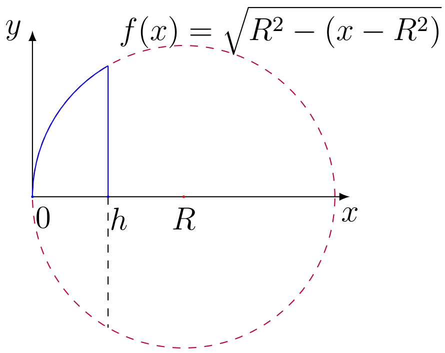

Figure A.2.: Function f for the sphere cap.

The lateral surface of spherical segments is equal if the height is equal, no matter where it were cut out of the sphere with radius R. This can be deduced by subtracting the surface area of two spherical caps with different height. The surface of a rotation body of height a is generally given by

$$M = 2\pi \int_0^a f(x) \cdot \sqrt{1 + f'(x)^2}\, \mathrm{d}x. \tag{A.7}$$

In this case, as illustrated in figure A.2, the function $f(x)$ is given by

$$f(x) = \sqrt{R^2 - (x - R^2)}, \quad f'(x) = -\frac{x - r}{\sqrt{R^2 - (x - R^2)}}. \tag{A.8}$$

Applying to (A.7) leads to

$$M_{\text{cap}}(a) = 2\pi \int\limits_0^a \sqrt{R^2 - (x - R^2)} \cdot \sqrt{1 + \frac{(x-r)^2}{R^2 - (x - R^2)}} \, \mathrm{d}x \tag{A.9}$$

$$= 2\pi \int\limits_0^a \sqrt{R^2 - (x - R^2) + (x - R^2)} \, \mathrm{d}x \tag{A.10}$$

$$= 2\pi R \int\limits_0^a \mathrm{d}x = 2\pi a R. \tag{A.11}$$

Now, the lateral surface of the spherical segment is the difference of the area of two spherical caps with a difference in height of $h := a - b$:

$$M_{\text{segment}} = M_{\text{cap}}(a) - M_{\text{cap}}(b) = 2\pi R(a - b) = 2\pi R h. \tag{A.12}$$

This formula only depends on the height of the spherical segment and the radius of the sphere. Therefore, the surface area is equal, no matter where it was cut out of the sphere.

A.3. Intersection point of line and cylinder and sphere

To calculate the way points in the tube and the hit points on the PMT, the intersections of a line with a cylinder and a sphere have to be calculated. As the calculation of both is very similar, this derivation focuses on the intersection points of the line with the cylinder.

A cylinder with the radius R and the height h can be described by the inequality

$$x^2 + y^2 = R^2, \tag{A.13}$$

$$0 \leq z \leq h. \tag{A.14}$$

The straight line g satisfies the equation

$$g : \begin{pmatrix} x \\ y \\ z \end{pmatrix} = \begin{pmatrix} s_x \\ s_y \\ s_z \end{pmatrix} + t \cdot \begin{pmatrix} d_x \\ d_y \\ d_z \end{pmatrix}, \tag{A.15}$$

where $\vec{s} = (s_x, s_y, s_z)^T$ is a vector pointing on an arbitrary point on the line, t is a real number and $\vec{d} = (d_x, d_y, d_z)^T$ is the direction vector of the line. To calculate the intersection points, equation (A.15) is applied into equation (A.13), which leads to the quadratic equation:

$$(s_x + t \cdot d_x)^2 + (s_y + t \cdot d_y)^2 = R^2 \tag{A.16}$$

$$\Leftrightarrow \underbrace{(d_x^2 + d_y^2)}_{a} t^2 + \underbrace{2(d_x s_x + d_y s_y)}_{b} t + \underbrace{s_x^2 + s_x^2 - R^2}_{c} = 0 \tag{A.17}$$

With the quadratic formula we can solve this for t:

$$t_{1/2} = \frac{-b \pm \sqrt{b^2 - 4ac}}{2a}, \tag{A.18}$$

with

$$\begin{aligned} a &= d_x^2 + d_y^2 \\ b &= 2(d_x s_x + d_y s_y) \\ c &= s_x^2 + s_x^2 - R^2. \end{aligned} \tag{A.19}$$

Therefore, the two intersection points are given by

$$\begin{pmatrix} x \\ y \\ z \end{pmatrix} = \begin{pmatrix} s_x \\ s_y \\ s_z \end{pmatrix} + t_{1/2} \cdot \begin{pmatrix} d_x \\ d_y \\ d_z \end{pmatrix}, \tag{A.20}$$

if z satisfies (A.14). Otherwise, at least one of the intersection points lies on covers of the cylinder. In this case, t can be determined by setting $z = z_{\text{cover}}$ (i.e. $z = 0$ or $z = h$) in the z component equation in (A.15) and solving for t:

$$t = \frac{z_{\text{cover}} - s_z}{d_z} \tag{A.21}$$

To get the corresponding intersection point, the new value of t can be applied as the second $t_{1/2}$ value in (A.20).

The intersection points of a sphere with a line can be determined analogously with the sphere equation

$$(x - x_c)^2 + (y - y_c)^2 + (z - z_c)^2 = R^2 \tag{A.22}$$

with the center at $\vec{r}_\mathrm{c}$ and the line described in equation (A.15). This results similar to equation (A.20) with the quadratic formula (A.18) in

$$\begin{pmatrix} x \\ y \\ z \end{pmatrix} = \begin{pmatrix} s_x \\ s_y \\ s_z \end{pmatrix} + t_{1/2} \cdot \begin{pmatrix} d_x \\ d_y \\ d_z \end{pmatrix}, \tag{A.23}$$

for the intersections of a sphere and a line. The parameters a, b and c differ from equations (A.19):

$$\begin{aligned} a &= \|\vec{d}\| \\ b &= 2 \cdot \langle \vec{d}, \vec{s} - \vec{r}_\mathrm{c} \rangle \\ c &= \|\vec{s} - \vec{r}_\mathrm{c}\| - R^2. \end{aligned} \tag{A.24}$$

As a sphere does not have covers as the cylinder, another distinction for special cases is not needed.

A.4. PMT radius formula

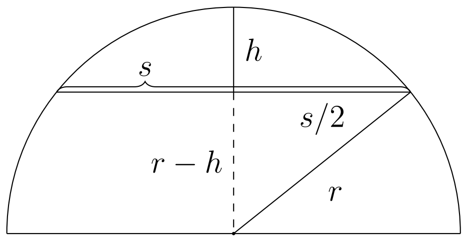

Figure A.3.: Designations for the circular segment

Here we want to determine the radius of the sphere with given parameters s and h of a circular segment. With the Pythagorean theorem and the designations in figure A.3, we can write

$$R^2 = (R - h)^2 + (s/2)^2 = R^2 - 2Rh + h^2 + \frac{s^2}{4} \tag{A.25}$$

$$\Leftrightarrow \qquad R = \frac{h^2 + s^2/4}{2h} \tag{A.26}$$

Simplifying the equation leads to the final formula

$$R = \frac{8h^2 + s^2}{8h}. \tag{A.27}$$

A.5. Distance of a point to a line

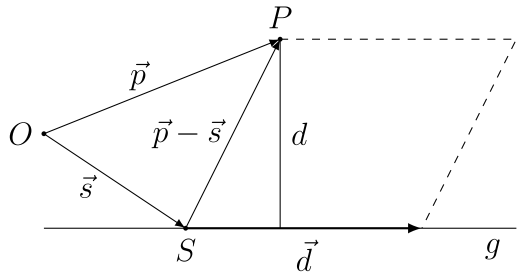

Figure A.4.: Distance of point to line

We want to determine the distance d of the point p to the line g. The distance is given by the length of the connection line between P and g, that stands perpendicular to g.

Let $\vec{p}$ be the vector pointing onto the point P and $g : \vec{s} + t \cdot \vec{d}$ the line. As shown in figure A.4, the difference vector $\vec{p} - \vec{s}$ and the direction vector $\vec{d}$ define a parallelogram, whose area equals the length of the cross product of $\vec{p} - \vec{s}$ and $\vec{d}$:

$$A_{\text{parallelogram}} = \|(\vec{p} - \vec{s}) \times \vec{d}\|. \tag{A.28}$$

On the other hand, the area of a parallelogram equals height times basic site. In this case, d is the height and the length of $\vec{d}$ is the basic site:

$$A_{\text{parallelogram}} = d \cdot \|\vec{d}\|. \tag{A.29}$$

Equating (A.28) and (A.29) and solving for d gives the short formula

$$d = \frac{\|(\vec{p} - \vec{s}) \times \vec{d}\|}{\|\vec{d}\|} \tag{A.30}$$

for the distance of a point to a line.

B. Data sheets

B.1. Hamamatsu R12860-50

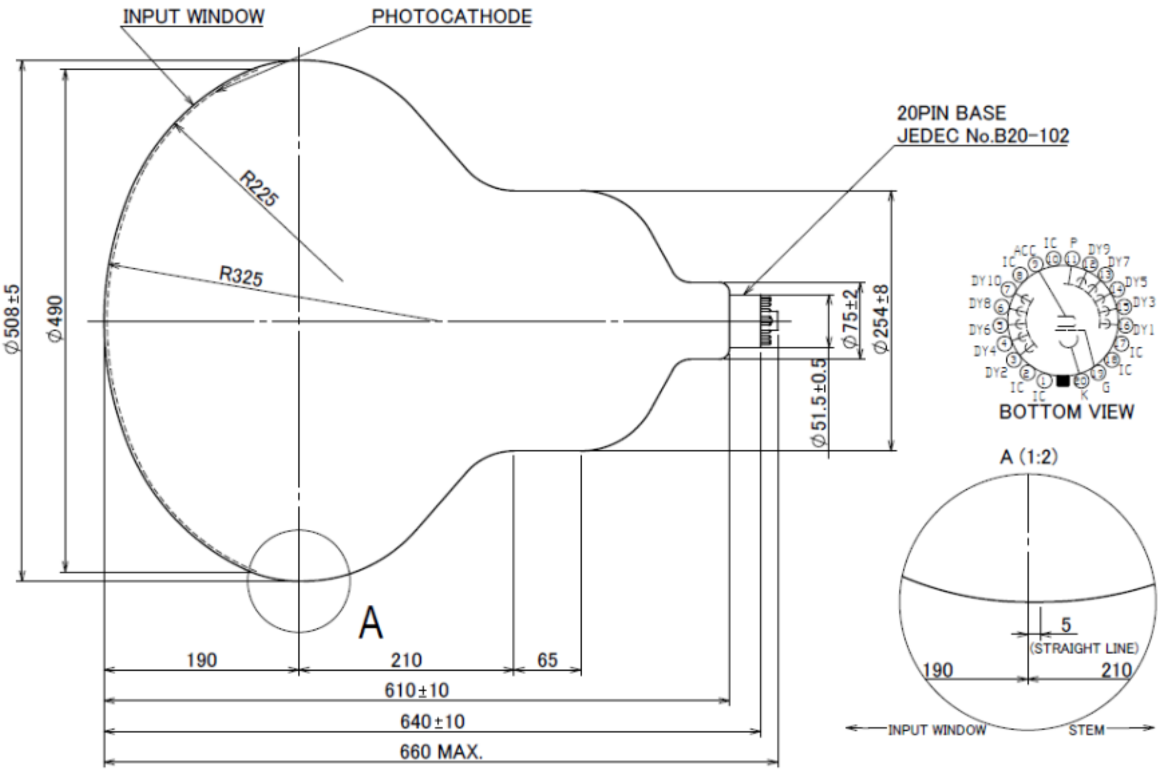

Figure B.1.: Geometry of the Hamamatsu R12860-50 photomultiplier [34].

B.2. MCP PMT

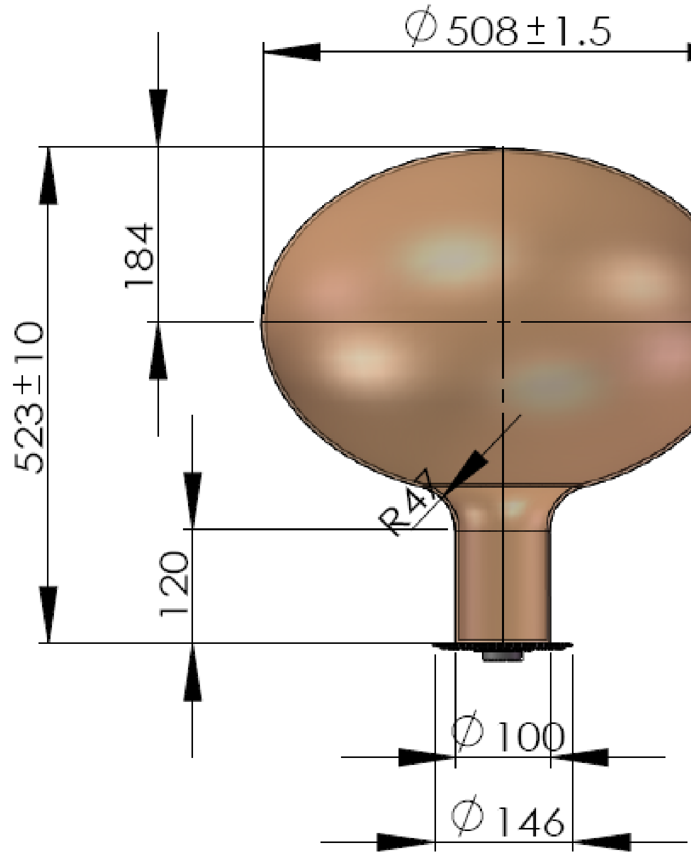

Figure B.2.: Geometry of the MCP photomultiplier [34].

C. Additional setups

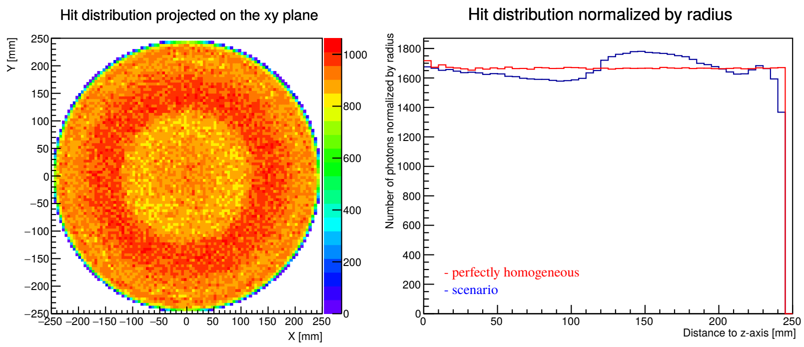

(a) 280 mm Tyvek

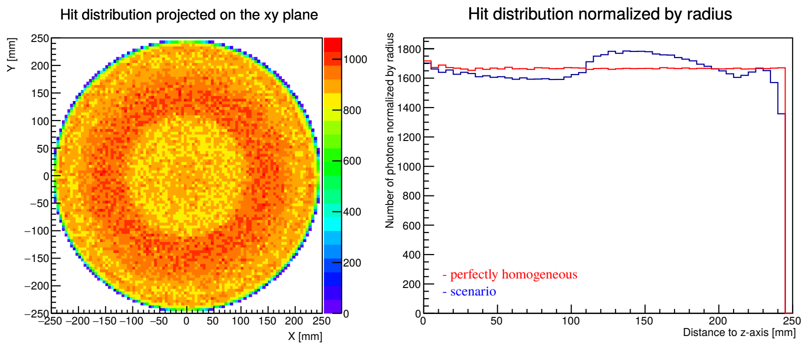

(b) 290 mm Tyvek

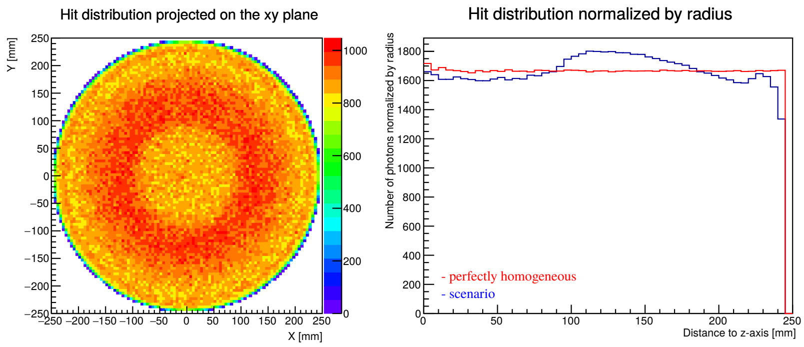

(c) 310 mm Tyvek

Figure C.1.: 280 to 310 mm Tyvek stripe without a diffuser.

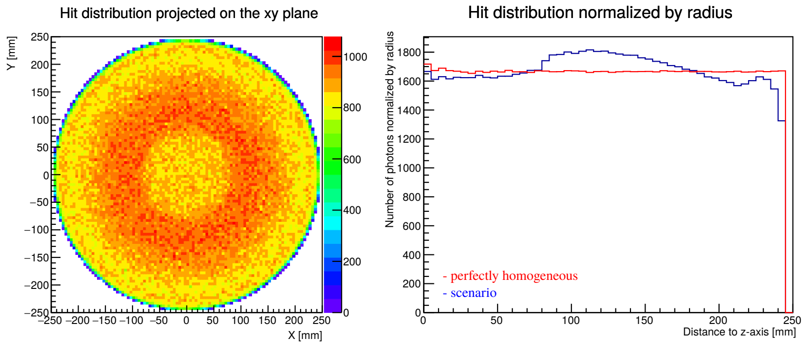

(a) 320 mm Tyvek

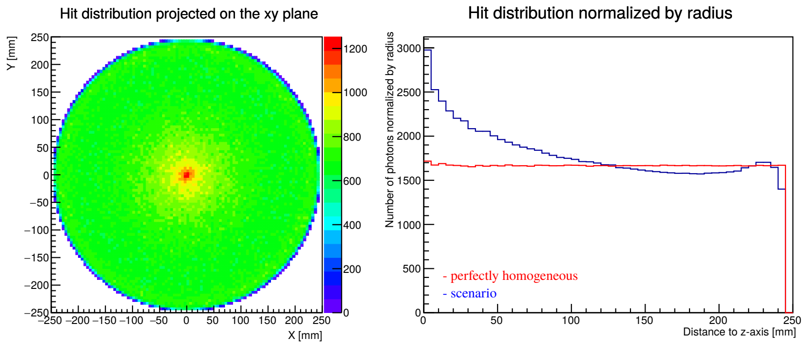

(b) 500 mm Tyvek

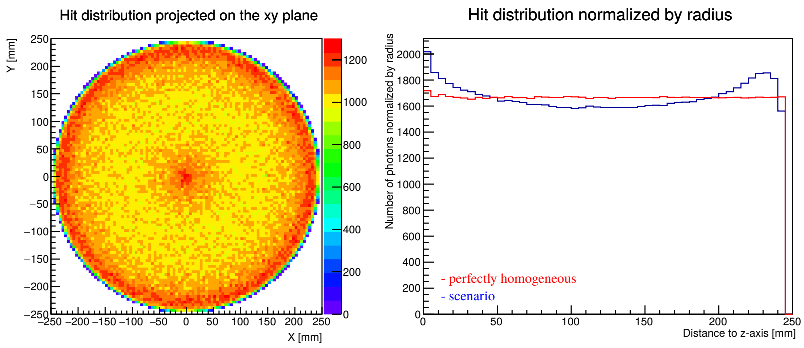

(c) 620 mm Tyvek

Figure C.2.: 320 to 620 mm Tyvek stripe without a diffuser.

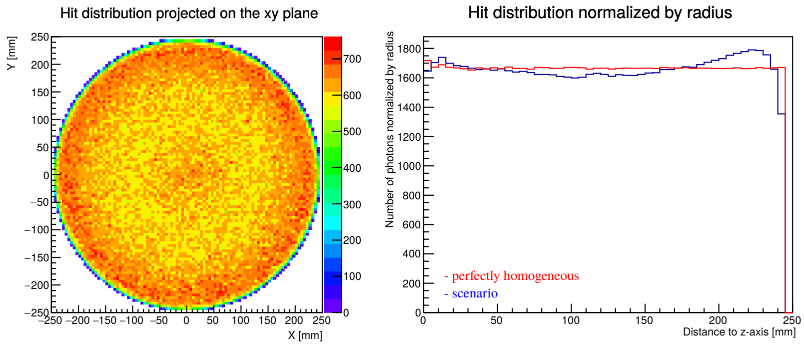

(a) Ideal diffuser

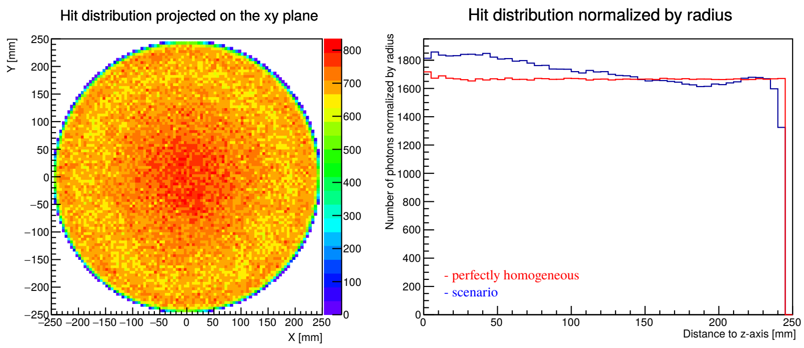

(b) Holographic diffuser with 80° opening angle

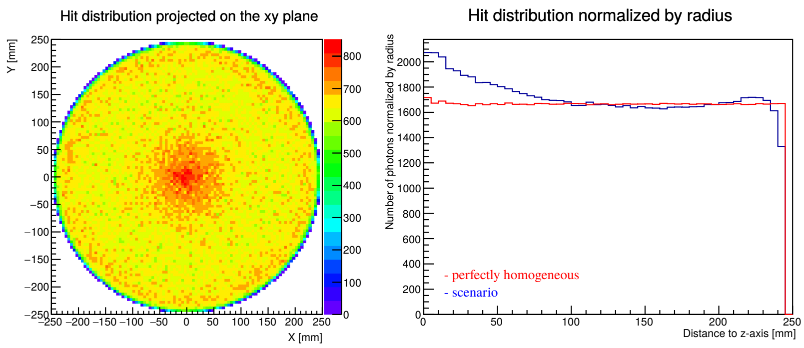

(c) Standard Diffuser with 70% scattering and 10° opening angle

Figure C.3.: 400 mm Tyvek stripe with different diffusers at 260 mm.

List of Figures

List of Tables

Bibliography

[1] S. Agostinelli et al. "Geant4—a simulation toolkit." In: *Nuclear Instruments and Methods in Physics Research Section A: Accelerators, Spectrometers, Detectors and Associated Equipment* 506.3 (July 1, 2003), pp. 250–303. ISSN: 0168-9002. DOI: 10.1016/S0168-9002(03)01368-8. URL: http://www.sciencedirect.com/science/article/pii/S0168900203013688 (visited on 09/19/2016).

[2] Fengpeng An et al. "Neutrino physics with JUNO." In: *Journal of Physics G: Nuclear and Particle Physics* 43.3 (Mar. 1, 2016), p. 030401. URL: http://stacks.iop.org/0954-3899/43/i=3/a=030401 (visited on 08/24/2016).

[3] Nikolai Anphimov. "Sampling test FDR - PMT sampling test by scanning station approach." In: July 27, 2016. URL: http://juno.ihep.ac.cn/cgi-bin/Dev_DocDB/ShowDocument?docid=1799 (visited on 09/18/2016).

[4] Akash Arora. *How to Use Luminit's LSD Model in OpticStudio*. June 29, 2016. URL: http://www.zemax.com/zmx/webinars/opticstudio-recordings/how-to-use-luminit%E2%80%99s-lsd-model-in-opticstudio (visited on 08/15/2016).

[5] Christian Blatter and joriki. *Generate a random direction within a cone*. 2012. URL: https://math.stackexchange.com/questions/56784/generate-a-random-direction-within-a-cone (visited on 08/21/2016).

[6] David-Samuel Blum. "Total intensity distribution on the PMT cathode." 2016.

[7] T. Briese et al. "Testing of Cryogenic Photomultiplier Tubes for the MicroBooNE Experiment." In: *JINST* 8 (July 23, 2013), T07005. DOI: 10.1088/1748-0221/8/07/T07005.

[8] Rene Brun and Fons Rademakers. *ROOT Data Analysis Framework - User's Guide*. May 2014. URL: https://root.cern.ch/root/htmldoc/guides/users-guide/ROOTUsersGuide.html (visited on 08/24/2016).

[9] DONUT Collaboration. "Observation of Tau Neutrino Interactions." In: *Physics Letters B* 504.3 (Apr. 2001), pp. 218–224. ISSN: 03702693. DOI: 10.1016/S0370-2693(01)00307-0. arXiv: hep-ex/0012035. URL: http://arxiv.org/abs/hep-ex/0012035 (visited on 09/10/2016).

[10] The ATLAS Collaboration. "Observation of a new particle in the search for the Standard Model Higgs boson with the ATLAS detector at the LHC." In: *Physics Letters B* 716.1 (Sept. 2012), pp. 1–29. ISSN: 03702693. DOI: 10.1016/j.physletb.2012.08.020. arXiv: 1207.7214. URL: http://arxiv.org/abs/1207.7214 (visited on 09/10/2016).

[11] C. L. Cowan et al. "Detection of the Free Neutrino: a Confirmation." In: *Science* 124.3212 (July 20, 1956), pp. 103–104. ISSN: 0036-8075, 1095-9203. DOI: 10.1126/science.124.3212.103. URL: http://science.sciencemag.org/content/124/3212/103 (visited on 09/10/2016).

[12] G. Danby et al. "Observation of High-Energy Neutrino Reactions and the Existence of Two Kinds of Neutrinos." In: *Physical Review Letters* 9.1 (July 1, 1962), pp. 36–44. DOI: 10.1103/PhysRevLett.9.36. URL: http://link.aps.org/doi/10.1103/PhysRevLett.9.36 (visited on 09/10/2016).

[13] Raymond Davis, Don S. Harmer, and Kenneth C. Hoffman. "Search for Neutrinos from the Sun." In: *Physical Review Letters* 20.21 (May 20, 1968), pp. 1205–1209. DOI: 10.1103/PhysRevLett.20.1205. URL: http://link.aps.org/doi/10.1103/PhysRevLett.20.1205 (visited on 09/10/2016).

[14] Zelimir Djurcic et al. "JUNO Conceptual Design Report." In: *arXiv:1508.07166 [hep-ex, physics:physics]* (Aug. 28, 2015). arXiv: 1508.07166. URL: http://arxiv.org/abs/1508.07166 (visited on 08/11/2016).

[15] E. Fermi. "Versuch einer Theorie der β-Strahlen. I." In: *Zeitschrift fur Physik* 88 (Mar. 1, 1934), pp. 161–177. DOI: 10.1007/BF01351864. URL: http://adsabs.harvard.edu/abs/1934ZPhy...88..161F (visited on 09/10/2016).

[16] Christian Gerthsen and Dieter Meschede. *Gerthsen Physik*. Springer-Lehrbuch. Berlin, Heidelberg: Springer Berlin Heidelberg, 2015. ISBN: 978-3-662-45976-8 978-3-662-45977-5. URL: http://link.springer.com/10.1007/978-3-662-45977-5 (visited on 09/10/2016).

[17] W. C. Haxton. "Neutrino Oscillations and the Solar Neutrino Problem." In: *arXiv:nucl-th/0004052* (Apr. 23, 2000). arXiv: nucl-th/0004052. URL: http://arxiv.org/abs/nucl-th/0004052 (visited on 09/10/2016).

[18] *JUNO*. 2016. URL: http://www.neutrino.uni-hamburg.de/projekte/juno/ (visited on 09/01/2016).

[19] Horst Kuchling. *Taschenbuch der Physik*. 20th ed. München: Carl Hanser Verlag GmbH & Co. KG, Nov. 4, 2010. 711 pp. ISBN: 978-3-446-42457-9.

[20] Jack B. Kuipers. *Quaternions and Rotation Sequences: A Primer with Applications to Orbits, Aerospace, and Virtual Reality*. Princeton University Press, 2002. 398 pp. ISBN: 978-0-691-10298-6.

[21] Johann Heinrich Lambert and E. (Ernst) Anding. *Lamberts Photometrie : [Photometria, sive De mensura et gradibus luminus, colorum et umbrae] (1760)*. In collab. with Harvard University. Leipzig : W. Engelmann, 1892. 433 pp. URL: http://archive.org/details/lambertsphotome00lambgoog (visited on 09/10/2016).

[22] *Layout of the JUNO detector*. 2016. URL: https://www.staff.uni-mainz.de/wurmm/wurm-home/juno-layout.png (visited on 08/30/2016).

[23] Yu-Feng Li. "Overview of the Jiangmen Underground Neutrino Observatory (JUNO)." In: *International Journal of Modern Physics: Conference Series* 31 (Jan. 2014), p. 1460300. ISSN: 2010-1945, 2010-1945. DOI: 10.1142/S2010194514603007. arXiv: 1402.6143. URL: http://arxiv.org/abs/1402.6143 (visited on 09/01/2016).

[24] Luminit. *Light shaping defusers - Technical datasheet*. May 21, 2012. URL: http://www.luminitco.com/tech_data (visited on 08/15/2016).

[25] Luminit. *Understanding light shaping diffusers*. June 4, 2012. URL: http://www.acalbfi.com/de/suppliers/HYS (visited on 08/15/2016).

[26] Makoto Matsumoto and Takuji Nishimura. "Mersenne Twister: A 623-dimensionally Equidistributed Uniform Pseudo-random Number Generator." In: *ACM Trans. Model. Comput. Simul.* 8.1 (Jan. 1998), pp. 3–30. ISSN: 1049-3301. DOI: 10.1145/272991.272995. URL: http://doi.acm.org/10.1145/272991.272995 (visited on 08/18/2016).

[27] Dario Motta and Stefan Schonert. "Optical properties of bialkali photocathodes." In: *Nuclear Instruments and Methods in Physics Research Section A: Accelerators, Spectrometers, Detectors and Associated Equipment* 539.1 (Feb. 21, 2005), pp. 217–235. ISSN: 0168-9002. DOI: 10.1016/j.nima.2004.10.009. URL: http://www.sciencedirect.com/science/article/pii/S0168900204022132 (visited on 08/04/2016).

[28] Libor Nozka et al. "BRDF profile of Tyvek and its implementation in the Geant4 simulation toolkit." In: *Optics Express* 19.5 (Feb. 28, 2011), pp. 4199–4209. ISSN: 1094-4087.

[29] K. A. Olive et al. "Review of Particle Physics." In: *Chin.Phys.* C38 (2014), p. 090001. DOI: 10.1088/1674-1137/38/9/090001.

[30] *Oszillation pattern of JUNO*. 2016. URL: http://www.neutrino.uni-hamburg.de/sites/site_neutrino/content/e45955/e245120/e262784/JUNO_Oszillation_Pattern.png (visited on 08/30/2016).

[31] M. L. Perl et al. "Evidence for Anomalous Lepton Production in $e^+ - e^-$ Annihilation." In: *Physical Review Letters* 35.22 (Dec. 1, 1975), pp. 1489–1492. DOI: 10.1103/PhysRevLett.35.1489. URL: http://link.aps.org/doi/10.1103/PhysRevLett.35.1489 (visited on 09/10/2016).

[32] Bogdan Povh et al. *Teilchen und Kerne: Eine Einfuhrung in die physikalischen Konzepte*. 8. Aufl. 2009. Berlin; Heidelberg: Springer, Mar. 6, 2009. 432 pp. ISBN: 978-3-540-68075-8.

[33] X. Qian and P. Vogel. "Neutrino Mass Hierarchy." In: *Progress in Particle and Nuclear Physics* 83 (July 2015), pp. 1–30. ISSN: 01466410. DOI: 10.1016/j.ppnp.2015.05.002. arXiv: 1505.01891. URL: http://arxiv.org/abs/1505.01891 (visited on 09/10/2016).

[34] Zhonghua Qin. "Geometry of Bare PMTs." 2016.

[35] Qwerty123uiop. *File:PhotoMultiplierTubeAndScintillator.jpg*. In: *Wikipedia, the free encyclopedia*. Nov. 3, 2013. URL: https://en.wikipedia.org/wiki/File:PhotoMultiplierTubeAndScintillator.jpg (visited on 08/30/2016).

[36] *Scheme*. 2016. URL: http://english.ihep.cas.cn/rs/fs/juno0815/Junojuno/Schjuno/201403/t20140306_117341.html (visited on 09/01/2016).

[37] Norbert Schmitz. *Neutrinophysik*. 1997th ed. Stuttgart: Teubner Verlag, Jan. 1, 1997. 484 pp. ISBN: 978-3-519-03236-6.

[38] Virginia Strati et al. "Expected geoneutrino signal at JUNO." In: *arXiv:1412.3324 [physics]* (Dec. 10, 2014). arXiv: 1412.3324. URL: http://arxiv.org/abs/1412.3324 (visited on 09/29/2016).

[39] Christoph Tornau. *Rotationsmatrix - Eigenschaften der Rotationsmatrix*. Aug. 15, 2016. URL: http://www.informatikseite.de/animation/node14.php (visited on 08/20/2016).

[40] *TRandom3 Class Reference*. Aug. 24, 2016. URL: https://root.cern.ch/doc/master/classTRandom3.html (visited on 08/24/2016).

[41] Yaoguang Wang. "Optical Simulation of PMT." In: May 13, 2016. URL: junodocdb.physik.rwth-aachen.de/DocDB/Dev_DocDB/0016/001629/001/Update%20of%20Optical%20Simulation%20of%20PMT.pdf (visited on 08/24/2016).

[42] Eric W. Weisstein. *Disk Point Picking*. URL: http://mathworld.wolfram.com/DiskPointPicking.html (visited on 09/12/2016).

[43] L. Wolfenstein. "Neutrino oscillations in matter." In: *Physical Review D* 17.9 (May 1, 1978), pp. 2369–2374. DOI: 10.1103/PhysRevD.17.2369. URL: http://link.aps.org/doi/10.1103/PhysRevD.17.2369 (visited on 09/04/2016).

[44] Björn Wonsak. "Status PMT mass testing." July 27, 2016.

[45] Liang Zhan. "JUNO: A Next Generation Reactor Antineutrino Experiment." In: *arXiv:1506.01152 [hep-ex, physics:physics]* (June 3, 2015). arXiv: 1506.01152. URL: http://arxiv.org/abs/1506.01152 (visited on 09/01/2016).

[46] Kai Zuber. *Neutrino Physics, Second Edition*. Revised. Boca Raton, FL: Routledge Chapman & Hall, Aug. 2, 2011. 466 pp. ISBN: 978-1-4200-6471-1.

Danksagung

Vielen Dank an alle, die beim Erstellen dieser Bachelor-Arbeit geholfen haben. Ich danke Prof. Dr. Caren Hagner für die Möglichkeit meine Bachelor-Arbeit in ihrer Arbeitsgruppe in einem spannenden Gebiet der Physik machen zu können.

Dr. Björn Wonsak für die Betreuung meiner Arbeit und die Geduld und Tiefe beim Beatworten meiner Fragen.

Henning Rebber nicht nur für die Korrektur und Tipps direkt zur Arbeit, sondern auch für die schnelle Hilfe bei Problemen jeglicher Art.

Hans-Jürgen "Hajo" Ohmacht für die umfangreiche Hilfe beim Bekleben der Röhren für den Testand.

Meinen Kommilitonen und Freunden Benedict für die LaTeX-Nachhilfe und Felix für die Ablenkung.

Allen im Büro für die Hilfe bei den zahlreichen ROOT und C++ Fragen und auch allen in der Arbeitsgruppe für das freundliche und unterhaltsame Arbeitsklima und natürlich für den Kuchen.

Außerdem möchte ich auch meiner Familie danken, die mir jederzeit beiseite stand und mich finanziell unterstützt hat. Besonders meinem Vater und meiner Schwester Caroline für die Verbesserung der sprachlichen Fehler und die allgemeine Anhebung der Verständlichkeit meiner Arbeit.

Erklärung

Hiermit bestätige ich, dass die vorliegende Arbeit von mir selbständig verfasst wurde und ich keine anderen als die angegebenen Hilfsmittel – insbesondere keine im Quellenverzeichnis nicht benannten Internet-Quellen – benutzt habe und die Arbeit von mir vorher nicht einem anderen Prüfungsverfahren eingereicht wurde. Die eingereichte schriftliche Fassung entspricht der auf dem elektronischen Speichermedium. Ich bin damit einverstanden, dass die Bachelorarbeit veröffentlicht wird.

Hamburg, den 02.11.2016

Simon Reichert